Munich University of Applied Sciences

Electrical Engineering & Information Technology

M.Sc. Electrical Engineering

Supervisor: Prof. Dr. Christoph M. Hackl

Analysis of Actuator Control Strategies for Excitation of Intrinsic Modes in Compliant Robots with Series Elastic Actuators

Master's Thesis

Author:

Filip Pasic

Supervisors at DLR:

M.Sc. Annika Schmidt

Dr. Manuel Keppler

Prof. Dr. Alin Albu-Schäffer

In cooperation with:

German Aerospace Center (DLR)

Institute of Robotics and Mechatronics

Start Date: 15.03.2023

Submission Date: 15.09.2023

Ifd. Nr. 817

Abstract

In biology, body dynamics and elasticity in periodic motions most likely contribute to efficiency, i.e., in mammalian locomotion. Likewise, elastic elements can be added to robotic systems in an attempt to mimic this biological concept. Compliant robots are less likely to get damaged after severe impacts and their mechanical energy storage via springs could be exploited for fast and explosive movements. In this thesis, we explore the question whether resonance excitation that solely considers link-side dynamics or also takes into account the motor inertia, can lead to an increase in performance in Series Elastic Actuator (SEA) driven robotic systems. We propose three different control approaches and compare them to compliant state-of-the-art control as baseline evaluation in simulation and hardware experiments. Moreover, we extend the investigation of motor-side-excitation with the aid of methods such as inertia shaping and simulative system variation. Experiment results regarding a pick-and-place task with fixed amplitude reveal that in the investigated test setup, it might not be beneficial to make dedicated use of the motor inertia. Instead, an approach that exclusively excites link-side dynamics appears, for this particular task and setup, to be advantageous. However, generally, also making use of the motor dynamics bears potential for specific investigations as it appears more flexible and the control behavior can be easily adapted. Thus, the presented thesis provides first fundamental insights about novel control strategies and lies the foundation for further systematic research with different actuation types and varying task goals.

Index Terms: Compliant Robots; Resonance Excitation; Pick-and-Place; Compliant Control Theory; Linear Modes; Inertia Shaping;

Contents

List of Figures

List of Tables

List of Symbols and Abbreviations

Abbreviations

DLR	Deutsches Zentrum für Luft- und Raumfahrt
RMC	Institut für Robotik und Mechatronik
SEA	Series Elastic Actuator
PBC	Passivity Based Control
VSA	Variable Stiffness Actuator
ESPi	Elastic Structure Preserving Impedance Controller
BB	Bang-Bang Control
DoF	Degree of Freedom
$1M$-T	1 Mass-Tracking
$1M-E$	1 Mass $ES\pi$-based Periodic Excitation
$2M-V$	2 Mass-Velocity Excitation
COM	Center Of Mass
PID	Proportional Integral Derivative Control
SOFTY	SEA-based robot with one link
DAVID	Anthropomorphic robot
EMA	Electro-Magnetic Actuator
DLR-LWR	DLR Light Weight Robot
FSJ	Floating Spring Joints
BLDC	Brushless DC Motor
1M	Link-side One Mass Resonance Control Approaches

1D/1M	One Dimensional Linear Mode Concept
2D/2M	Two Dimensional Linear Mode Concept with Motor Inertia Influence

Signals

u	Control Torque Input
θ	Motor Position Measurement after Gear-system
$\dot{\theta}$	Motor Velocity
$\ddot{\theta}$	Motor Acceleration
q	Link Position Measurement
$\dot{q}$	Link Velocity
$\ddot{q}$	Link Acceleration
$\dddot{q}$	Link Jolt
q_d	Desired Link Position of Tracking Control
τ	Spring Torque Signal
τ_{msr}	Sensor based Measurement of Spring Torque Signal
f_q	Link-side Velocity Excitation
f_{q-1D}	One-dimensional Energy-based Velocity Excitation
θ_d	Desired Motor Position Excitation via Transformation Equation
E_{msr-1D}	One-dimensional Energy Calculation for $1M$-T
E_{msr-2D}	Two-dimensional Energy Calculation
ξ_{com}	Center of Mass
$\tilde{\xi}_{com}$	Center of Mass Control Error
ξ_{PID}	PID-based Signal via COM Calculation
$\tilde{E}$	Energy Control Error
$\hat{Q}_a$	Friction Observer Estimation

1 Introduction

Stiff actuated robots are commonly used throughout industry and research settings with remarkable precision and rapid response time, thus making them indispensable across a broad integration-spectrum [1] [2], starting from industrial automation and micro/nano manipulation up to medical robots (e.g. surgical application, rehabilitation in physical therapy) [3] [4] [5]. As undisputed as their advantages may be, stiff robots are prone to damage when falls occur [6], especially in the field of mobile robotics for rough-terrain exploration, where falling is a necessity in the learning process of walking [7] [8] [9] [10] [11]. Inspired by nature, adding flexibility to mechanical systems allows to store and reuse energy (Figure 1.1). Yet, this new feature directly leads to more sophisticated systems with the necessity of innovative control approaches [12]. One approach to stabilize and exploit elastic systems is by applying controllers that support intrinsic motions of a system [13]. As the controller is in this case aiding the motion that the system is inherently inclined to do, this approach is promising to develop strategies that are energy efficient [14]. So far, such excitation strategies have mainly been investigated by taking into account the link-side dynamics of robotic systems, yet ignoring the motor-dynamics [15]. However, the motor-dynamics play a crucial role in regards of the overall system dynamics and should be considered when dynamical control approaches are explored. The presented master thesis aims to address this shortcoming and investigates whether compliant robots can benefit from exploiting both the eigendynamics of the link-side and the motor dynamics in our control strategy.

The core of this thesis, is the investigation of three different control approaches to perform a defined motion task on a single joint with an Series Elastic Actuator (SEA). Two of the controllers only excite the link-side dynamics, while the third

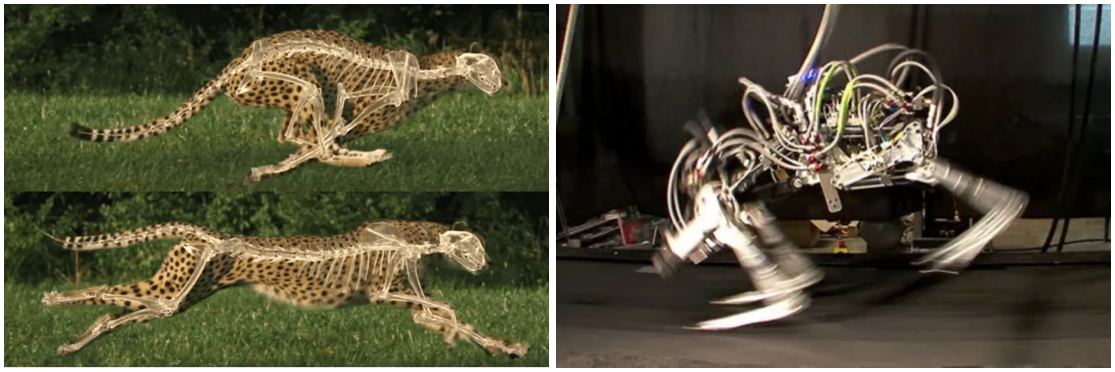

Figure 1.1: Running movement depiction of a cheetah (*left*) with a flexible spine illustration by actively bending and stretching for agile locomotion and a biologically inspired Boston Dynamics' Cheetah Robot (*right*), adapted from [16] [17].

one considers both the link-side and motor dynamics. The three controllers will be compared with respect to their energy/ power consumption to excite the defined motion. As baseline for the comparions, the Elastic Structure Preserving Impedance Controller (ESPi) [12] method is additionally implemented.

To provide a solid foundation, we first introduce relevant theory (Chapter 2), which covers topics such as compliance in robotics, mathematical SEA design, control, linear modes and the concept of inertia shaping. The theoretical groundwork is followed by detailed derivation of the three investigated control concepts (Chapter 3). All controllers are implemented in a hardware setup consisting of a single SEA actuated link, on which first a characterization is carried out. Following that, experiments with a defined control task for the three controllers and the ESPi as baseline are carried out to compare the perfomance (Chapter 4). Triggered by the findings of the initial experiment, we deepen the investigation of motor inertia influence on the third control strategy (Chapter 5).

Finally, all results will be discussed (Chapter 6) and the main findings summarized in a conclusion (Chapter 7).

2 State of the Art

This chapter will introduce the current state of the art relevant for this thesis. This includes an overview of why and how elasticities are added to robotic systems, as well as strategies to control such systems. Additionally, a short introduction to mode theory and the concept of inertia shaping is given.

2.1 Elasticities in Robotic Systems

Scientific robotics research strives to match biological behaviour in terms of motion, efficiency, redundancy and automization techniques [16] [14] [18] [12] [19]. As control techniques and hardware development continously improve, embedment of elasticities is successively gaining attention through its potential to increase the robustness of systems and store energy elastic elements. They allow robots to fall down, by cushioning the system after severe impacts. Permitting them to do so without being broken, enhances the progression of robotics development. Therefore, implementation of physical compliance in robots can be advantageous, especially if sensors or control fail at fast movements.

When talking about elasticities in robotic Electro-Magnetic Actuator (EMA) systems, we have to differentiate between various actuator concepts and design approaches to achieve this status.
We introduce three commonly known methods for elasticity in robots: 1) Series Elastic Actuators (SEAs) where motor and link are physically decoupled by a spring, 2) Variable Stiffness Actuators (VSAs) with variable stiffness in a spring-decoupled system and 3) proprioceptive actuation, where internal sensors lead to *self-awareness* of the robot when external forces are *sensed* with physical compliance

being integrated in mechanical mechanisms such as legs or arms.

In SEAs, the motor torque is directly passed onto the spring and then only relayed to the link. This concept establishes mechanical buffers for motors and severe impacts on the link, but requires complex control strategies and reliable sensors.

VSAs are often designed based on the concept of SEAs with adaptable stiffness as the characterstic key element. Changing the stiffness during movement allows the system to adapt to different tasks and conditions, thus mimicking the behaviour of biological muscles. For this reason, this actuation concept is often used for *anthropomorphic* robots.

For the proprioceptive actuation no physical compliance is added in the actuator chain itself, but instead integrated in the system through a sensor-based *self-awareness* [20]. Mechanical compliance is reached through implementation of flexible components in its links and control is adjusted properly when external forces are encountered. Hence, this enables the robot to mimick biological behaviour. Proprioceptive actuation of the robot MIT Cheetah 3 [20] [21] for example represents a counter part to SEA/ VSA driven systems, where flexibility is positioned outside of the drivetrain and mainly realized through a combination of flexible leg-elements. Cushioning of the motor unit, is achieved mainly through control, sensors and its inherent body flexibility. Since the motor torque is not transitioned to a spring, the force bandwidth of proprioceptive actuators can be greater, compared to SEA driven systems [20] [22].

Figure 2.1 shows an illustration of a conceptual compliant hand-arm robot with its SEA joint, where upper- and lower-arm are decoupled by a spring, which yields to the depicted control schematic.

Figure 2.2 and 2.3 both show compliant quadruped robots with different compliancy integration. First one depicts the DLR Bert [24] in rough terrain with integrated SEAs and second one MIT Cheetah 3 [21], with flexible legs and proprioceptive actuation, jumping on a desk.

Figure 2.4 shows an integration of VSAs in the humanoid robot David [25], where mechanically adjustable springs are located in the drive train. The *stiffness*

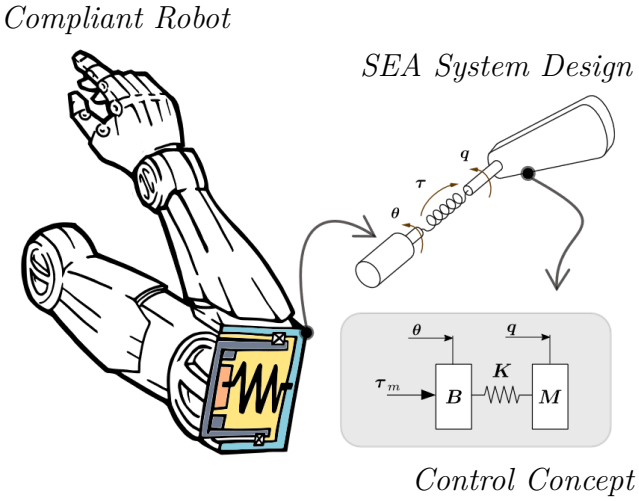

Figure 2.1: Illustration of a compliant SEA hand-arm design and its abbreviated concept of control, adapted from [23].

motor in the Floating Spring Joints (FSJ) [25] adjusts the stiffness of the nonlinear elastic element according to its control-task.

SEAs and VSAs are able to provide physical motor cushioning, which especially is advantageous in rough situations and difficult terrain, when e.g. sensors or control systems fail, making them especially promising concepts for locomoting robots. Moreover, due to the ability of storing energy in their springs (DLR Bert) or legs (Cheetah 3) SEAs, VSAs [25] and proprioceptive actuators [22] are enhancing robustness and enabling high-explosive movement tasks in robotic systems [26] [12]. Although SEAs, VSAs and proprioceptive actuators offer a large spectrum of benefits, they come with increased complexity, especially in control. This is due to the reason that those systems come with mechanical complexity, where both positions and forces have to be controlled properly (in a fast manner) and a discrepancy between motor position and link position needs to be accounted for. This opens up a large field of relevent topics for mastering this difficulty, such as: nonlinear eigendynamics, stability analysis, sensor-integration, real-time-processing, advanced control techniques by staying as close as possible to the natural behaviour of the system, exploitation of eigendynamics in general. In this thesis, the focus will lie on SEA-driven systems, with a particular focus to exploit the eigendynamics to

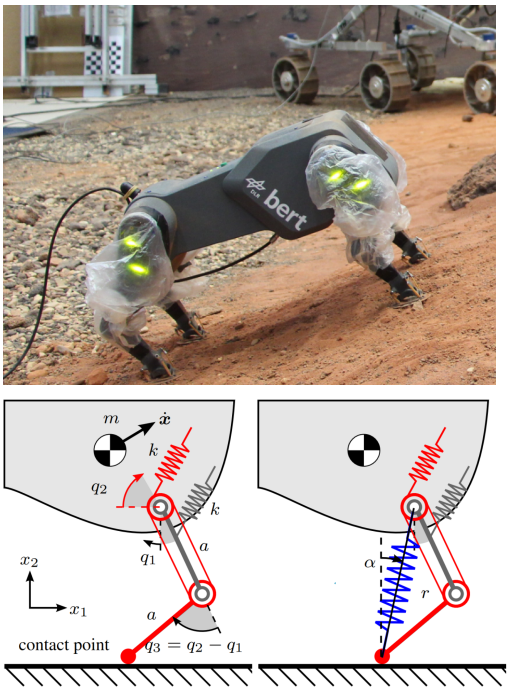

Figure 2.2: DLR Bert (top) with its compliant leg actuation (bottom), adapted from [24].

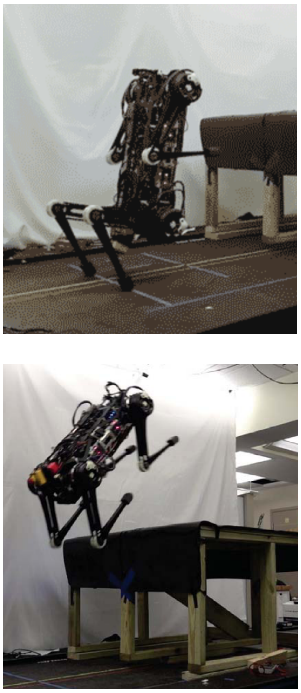

Figure 2.3: MIT Cheetah 3 jumping ($\approx 75cm$) on a desk, adapted from [22].

increase efficiency. The following sections will first introduce state-of-the-art control strategies for a single joint SEA system, followed by an opening for fundamentals of eigendynamics relevant for such a system.

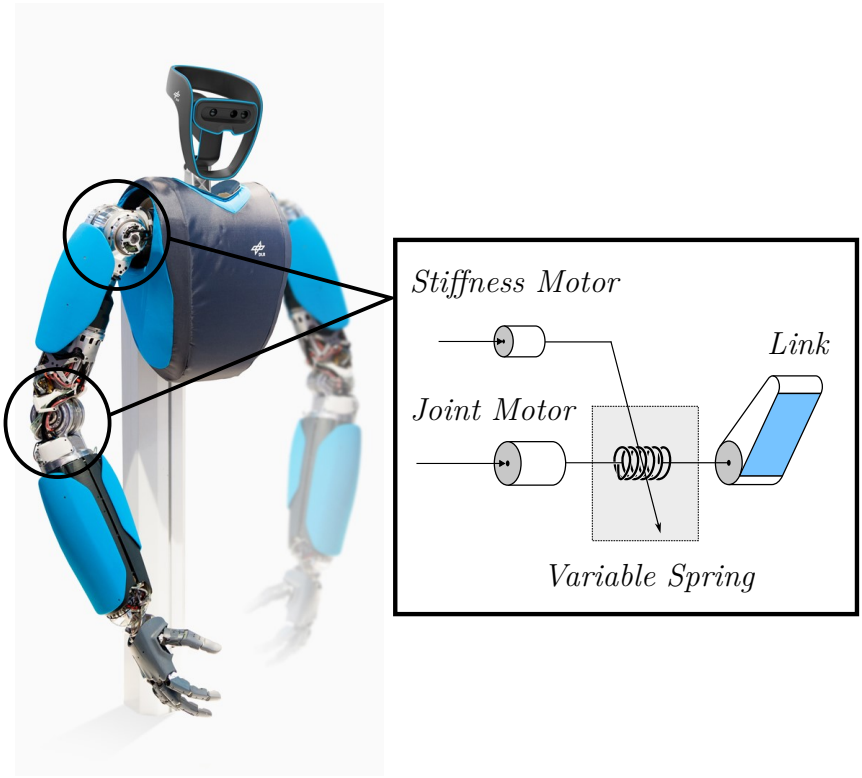

Figure 2.4: Anthropomorphic robot (DAVID) with its respective *joint motors* for compliant actuation in its VSAs, where variable stiffness of the nonlinear elastic element is adjusted via the *stiffness motors*.

2.2 Control of Elastic Robots

Although adding elasticity to a system through the integration of an SEA can increase robustness, it directly leads to more complex control, as depicted in Figure 2.5 where the link is physically decoupled from the motor. Thus, direct actuation of the link is not possible and the introduced dynamics by the spring require proper damping control. The focus of this thesis lies on investigating the potential of SEA-driven systems. Following the SEA structure and the elastic characteristics of a spring, this automatically introduces oscillatory dynamics in the plant [12]. At the same time, motor and link are being decoupled from each other, which directly results in an under-actuation of the link. Non-compliant robots are usually fully-actuated, with transmission of the motor being directly

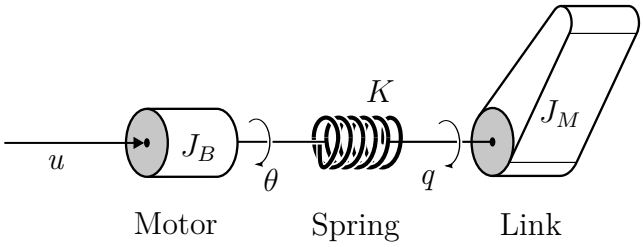

Figure 2.5: Schematic of a single SEA.

tranferred to the link, causing no difficulties in this regard. However, for the control of SEA systems, this has to be adapted properly in order to match this SEA based under-actuation of the system.

In this section, we will first briefly introduce the mathematical representation of an SEA link, followed by state-of-the-art approaches to control them by accommodating for the above mentioned challenged.

In the described SEA (Figure 2.5), J_B and J_M represent the motor- and link-inertia respectively, with θ and q as their corresponding position variables, u as the torque input to the motor and K as the spring stiffness. Thus, the spring exerts a force τ according to

$$\tau = K\ (\theta - q) \tag{2.1}$$

A model for the flexible joint can be derived by solving the Langrangian Equations via the energies for the appropriate matrix properties, yielding to the equations of motion for robots with multiple joints [27] [28]

$$M(q)\ddot{q} + C(q,\dot{q})\dot{q} + g(q) = \tau + L_{ex}\ , \tag{2.2}$$

$$B\ddot{\theta} + \tau = \tau_B\ . \tag{2.3}$$

where $M(q)$, $C(q,\dot{q})$, B represent the link-side inertia, the coriolis and the motor inertia matrix respectively. Gravity is denoted by the vector $g(q)$ and the external torques applied on the link are depicted as L_{ex}. The applied forces on

the rotor of the motor result in the depicted motor torques τ_B. Since the testbed possesses one joint, multi-Degree of Freedom (DoF) standard theory is not applied. Besides, the robot is horizontally actuated with no manually external force L_{ex} being applied on the link. For this reason, coriolis-, centrifugal-, gravitational- and external forces on the link can be ignored.

Let us propose an abbreviated version of the characteristic equations of motion in (2.2) and (2.3), by postulating

$$J_M \ddot{q} = K (\theta - q) , \tag{2.4}$$

$$u = J_B \ddot{\theta} + K (\theta - q) . \tag{2.5}$$

Here, these equations of motion are considerably shortened, according to the characteristics of the investigated robot. Due to its implementation and environmental contact in this thesis, some of the physical properties of the traditional equations of motion (2.2) and (2.3) can be neglected. We will focus on the equations (2.4) and (2.5) as a foundation of the controller design throughout this thesis.

One way to overcome the challenges introduced through spring decoupling in an SEA and the under-actuation of the link, is a Passivity Based Control (PBC) approach via motor-side control [29] [30] (Figure 2.6). The aim of this control approach is to acquire link-side damping and tracking behaviour with minimal influence on the plant dynamics.
This system requires a link-side tracking error

$$\tilde{q} = q - q_d(t) \tag{2.6}$$

where the desired link position is regulated via a time dependent variable $q_d(t)$ and the damping coefficient D suits its purpose with correspondence to the link-side tracking error, in order to fulfill $\tilde{q} \to 0$ tracking. This design requires motor-side impedance ($K_p\eta$ & $K_D\dot{\eta}$) with the declaration of a new virtual motor coordinate η in order to process the link-side damping and follow the desired trajectory. Details about this feature will be explained in the following.
The PBC allows to establish impedance, but comes at cost of decreased elasticity,

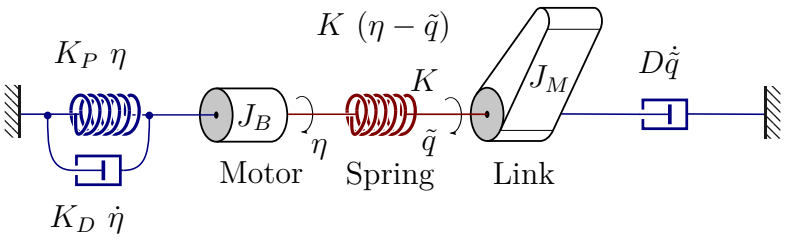

Figure 2.6: Illustration of the PBC for motion tracking and damping assignment.

due to the original characteristics of the SEA plant being not preserved. The reason behind this is that link-side damping is achieved through indirect damping control via the motor-side and not directly via the link-side [12]. This performance issue can be surpassed, by trying to adjust the control behaviour more to the original behaviour of the SEA by preserving its plant. Therefore, recent innovative research at Deutsches Zentrum für Luft- und Raumfahrt (DLR) Institut für Robotik und Mechatronik (RMC) developed a new control approach preserving the elasticity and keeping a dynamical behaviour of the link via the Elastic Structure Preserving Impedance Controller (ESPi) [12].

Figure 2.7 demonstrates the ESPi control with link-side impedance by obtaining the structure of the plant-dynamics. The desired system requires an introduction of a virtual motor coordinate η, yielding to a new expression of the spring deflection $K(\eta - q)$. In addition, viscous damping on motor-side with $D_\eta \dot{\eta}$ is introduced, which makes it possible to damp the plant proportionally to the motor velocity. A new spring K_q and damper D_q are proposed to realize link-side impedance with a desired link-position q_d. Hence, the proportional and derivative control can be expressed with $K_q(q - q_d)$ and $D_q \dot{q}$.

Characterizing the link mass dynamics of the original system (Figure 2.5) combined with the desired impedance control (Figure 2.7), according to Keppler et al. (2018) [12], yields

$$\underbrace{K(\theta - q)}_{\text{original system}} = J_M\ \ddot{q} = \underbrace{K(\eta - q) - D_q \dot{q} - K_q(q - q_d)}_{\text{desired system}} \tag{2.7}$$

By equating the original and desired link mass dynamics, a solution for the

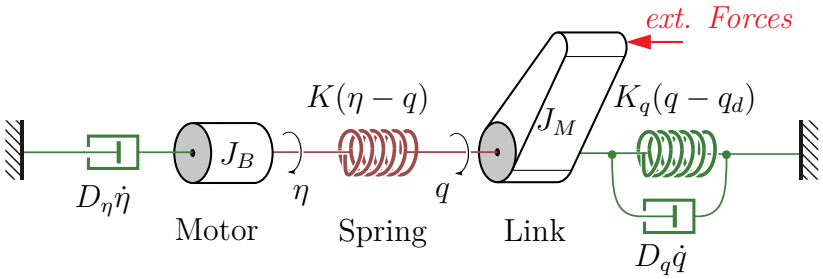

Figure 2.7: Illustration of the ESPi controller with link-side impedance, [12] adapted.

desired motor coordinate with respect to the virtual motor coordinate η and desired equilibrium point of the link q_d can be found. Equation (2.7) now leads to the transformation equation by solving for η

$$\eta = \theta - K^{-1}(-D_q\dot{q} - K_q(q - q_d)) \tag{2.8}$$

Including deliberately the earlier proposed viscous damper $D_\eta\dot{\eta}$ into the desired motor dynamics as control input, leads to the main equation of the original motor dynamics (Figure 2.5) and desired one (Figure 2.7)

$$\underbrace{J_B\ddot{\theta} + K\theta - u}_{\text{original system}} = Kq = \underbrace{J_B\ddot{\eta} + K\eta - D_\eta\dot{\eta}}_{\text{desired system}} \tag{2.9}$$

By inserting (2.8) into (2.9) the ESPi control law can be computed as

$$u = BK^{-1}(-D_q\dddot{q} - K_q\ddot{q}) - D_q\dot{q} - K_q(q - q_d) - D_\eta\dot{\eta} \tag{2.10}$$

As defined by [12], let the resulting closed loop dynamics be defined as

$$J_M\ \ddot{q} = K(\eta - q) - D_q\dot{q} - K_q(q - q_d)\ , \tag{2.11}$$

$$J_B\ \ddot{\eta} + K(\eta - q) = u_{visc-damp} = -D_\eta\dot{\eta}\ . \tag{2.12}$$

With respect to its preserved flexibility, the ESPi controller manages to damp proportional to its velocity on the motor-side and acquires link-side impedance behaviour. Thus, dominated K_q elasticity and D_q damping enables the system

to perfectly compensate external forces in its environment, while preserving a valuable degree of elasticity [12]. The efficiency of this control strategy in real compliant robots has been successfully shown in multiple applications [31] [32] [33].

Another control approach of elastic actuators with underactuated characteristics is proposed by [34], introducing a human based generation of cyclic motions (Bang-Bang Control (BB)).
Consider the earlier defined spring torque of (2.1) and satisfying the torque state evaluation discontinously [35] [34] with

$$u = \begin{cases} +\hat{\theta} & if\ \tau > \epsilon \\ 0 & if\ -\epsilon \leq \tau \leq \epsilon \\ -\hat{\theta} & if\ \tau < -\epsilon \end{cases} \tag{2.13}$$

The spring torque τ is compared to a fixed threshold value ϵ and a new motor step position $\hat{\theta}$ is commanded. Based on a state-evaluation of torque feedback, the motor-position is switched accordingly in order to create intrinsic oscillatory motions. As the link passes its equilibrium point in rotation, lost energy of one cycle is fed back into the system. Note that this is a linearized assumption and for nonlinear systems conditionally true. Nevertheless, it has proven as a reliable and robust concept in various experiments from the past [35] [36].

One great advantage of compliant systems is harnessing stored energy in springs to realise highly explosive movements (i.e. running, throwing and jumping). Braun et al. (2011) investigated the coordination of motion for a ball-throwing task, by exploiting a specific impedance profile for highly compliant systems with VSAs [26]. Figure 2.8 shows the Compliant Robot Design, the VSA and the according task for the robot. Each joint contains one VSA, which is capable of concurrently changing the equilibrium position (*SERVO 1*) and linear stiffness (*SERVO 2*) of the torsion spring. Braun et al. (2011) define the differential equations in state space and depict an optimization criterion to find a suitable control law. For solving the non-quadratic quality functional and including the nonlinear plant dynamics, the iterative linear quadratic regulator (iLQR) method is used. The *task* figure shows the movement of the robot arm. At the peak of its acceleration the ball is

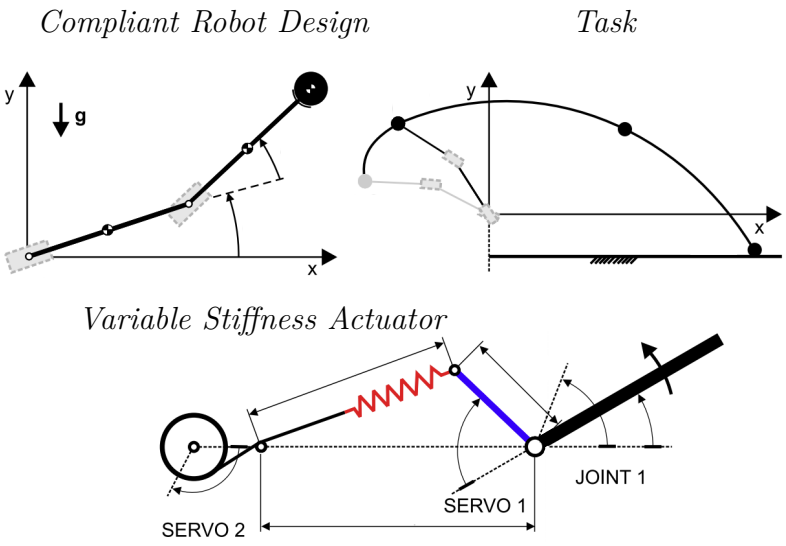

Figure 2.8: Depiction of the compliant robot design for a ball throwing experiment as an explosive task (*left*), the robot possesses VSA joints and releases the ball at peak acceleration (*right*) and the VSA design with two servo drive units for concurrently changing stiffness and equilibrium point of the spring (*bottom*), adapted from [26].

detached for a throw. This optimization lead to an increase of a 2 meter distance in ball throwing, by simultaneously optimizing torque and stiffness of the springs during motion, compared to utilizing fixed stiffness only. This evidence directly concludes better performance of compliant robots when control is matched with the respective eigendynamics of motion.

These findings are in line with the stated goal of this thesis, to investigate the efficiency of different control approaches that exploit these intrinsic dynamics in compliant systems. However, especially for more complex systems, it is not trivial to derive the eigendynamics and develope an appropriate control strategy. Recent work at DLR has extended the theory about intrinsic motions (i.e. eigenmodes) to be applicable for the nonlinear case, yet this topic in its entirely is very complex. Therefore, the scope of this thesis is limiting the system to the linear case with one SEA joint, to tackle the challenge of finding and understanding controllers that are suited for excitation of oscillatory motions in compliant systems.

2.3 Introduction to Linear Mode Theory

The following introduction is based on the classical dynamics in [37] [38] and introduction to (nonlinear) modes in [39]. Linear modes and oscillations cover a large application field i.e. molecular, solid-state physics and field theory [37]. Besides, one can find *normal modes* in a variety of different applications and systems, especially in the engineering domain. We refer to *normal modes*, when all components of a system are sinusoidally excited and reach the characterstic *eigenfrequency* of the total system. Usually, this is something we want to prevent in our designing process, e.g. bridges, machines, noise vibrations. However, in compliant robotics, there might actually lie potential in exploiting the eigendynamics of a system, i.e., by charging a spring element to jump higher or minimizing control effort by using the intrinsic motion of the system. Thus, understanding and shaping normal modes in robotic systems can inspire new control approaches and potentially improve and extend the application field of compliant robots drastically.

To derive the linear normal modes of a mass-spring-system, we can regard the involved energies. Consider the Euler-Langrangian $L \equiv T - V$ equation with its kinetic (T) and potential (V) part. Since stable equilibrium positions are the key factor for linear oscillation systems, we refer to those positions in a dynamical system as q_0. Therefore, the overall link position can be defined with $q = q_0 + x$, where x represents a small displacement from q_0. One can solve the oscillation with the Taylor Linearization Method ($V(q)$) by finding the minimum at q_0 of q, with

$$V(q) = V(q_0) + V'(q_0)x + \frac{1}{2}V''(q_0)x^2 + ... \tag{2.14}$$

Since q_0 already represents the minimum of V, the first derivative part $V'(q_0)x$ can be removed. Following the same procedure for the kinetic energy with $\zeta(q)$ as some function of q, under the consideration of $\dot{q} = \dot{x}$, the approximation of the Langrangian expression becomes

$$L \approx \frac{1}{2}\zeta(q)\dot{q} - \frac{1}{2}V''(q_0)x^2 - V(q_0) \equiv \frac{1}{2}m\dot{x} - \frac{1}{2}kx^2 - V(q_0) \tag{2.15}$$

By solving the derivatives of the Euler-Langrangian Method, we receive the

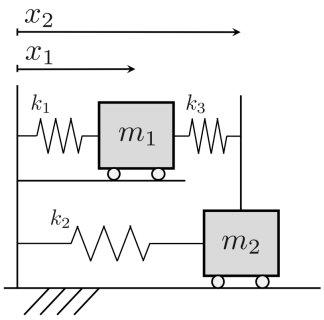

Figure 2.9: Illustration of a linear system with two DoFs, adapted from [39].

second-order equation of motion, which also directly reveals us the circular frequency f_{Hz}.

$$\ddot{x} + km^{-1} = 0 \longrightarrow \ddot{x} + (f_{Hz})^2 x = 0 \tag{2.16}$$

We introduce the *normal modes* with a state space example from [39].

In Figure 2.9, two masses are connected to a spring and the system has two DoFs with parallel movement enabled. The masses m_1 and m_2 are connected to each other through linear springs k_1, k_2, k_3. Consider x_1 and x_2 as the positions of the two masses, respectively. The linear mechanical system is defined with the time evolutions $x \ : \mathbb{R} \to \mathbb{R}^n$, where the potential field is quadratic and all functions fulfill a set of ordinary differential equations [39].

The system dynamics of the 2-DoF spring-mass system can overall be defined as $M\ddot{x} + Kx = 0$, with M as the inertia matrix and K as the stiffness matrix. In this case we extend the linear proposed system in (2.16) to a 2x2 system. By defining the given parameters $k_1 = \alpha(1+\delta)$, $k_2 = \alpha k$, $k_3 = k$, $m_1 = (1+\delta)m$, $m_2 = m$ with $\delta > -1$, $\alpha > 0$, $k > 0$, $m > 0$, the differential dynamic equations of the presented linear system can be described in state space as

$$m \begin{bmatrix} 1+\delta & 0 \\ 0 & 1 \end{bmatrix} \begin{bmatrix} \ddot{x}_1 \\ \ddot{x}_2 \end{bmatrix} + k \begin{bmatrix} 1+\alpha(\delta+1) & -1 \\ -1 & 1+\alpha \end{bmatrix} \begin{bmatrix} x_1 \\ x_2 \end{bmatrix} = \begin{bmatrix} 0 \\ 0 \end{bmatrix} \tag{2.17}$$

A closer examination of the exemplary state space system points towards a linear

superposition of motions, which can be scrutinized by calculating the *normal modes* via the corresponding eigenspaces. To find those, one has to uncouple the oscillators to find linear combinations of x. Let us change the earlier proposed equations of motion in (2.16) and satisfy the 2x2 system with $\Lambda \equiv M^{-1}K$. Since finding the eigenvectors requires the diagonalization of Λ, when at the same time a M^{-1} solution exists, we can solve the characteristic eigenvalue equation with

$$\Lambda\, x \;=\; \lambda\, x \tag{2.18}$$

in order to get

$$\ddot{x} \;=\; -\lambda\, x \equiv -(f_{Hz})^2\, x \tag{2.19}$$

The normal frequencies represent the square roots of the eigenvalues ($f_{Hz} = \sqrt{\lambda}$) [37]. Hence, the normal modes are described via the complex exponentials of the respective eigenvalues. Solving the eigenvector problem gives us the solutions for our two normal modes

$$x_2 \;=\; x_1\ , \tag{2.20}$$

$$x_2 \;=\; -(1+\delta)\, x_1\ . \tag{2.21}$$

In the first normal mode x_1 equals x_2, with both variables being positive, resulting in an in-phase vibration of the masses, as depicted in Figure 2.10 a). The second normal mode on the other hand shows 180° out of phase behaviour, see Figure 2.10 b). In [39], the mass distribution between m_1 and m_2 is tweaked to analyze two cases: $(m_1 = m_2)$ & $(m_1 > m_2)$. In the first case, phasic and anti-phasic result in equal amplitudes for x_1 and x_2, but for the second case the behaviour differs. The phasic trajectories are amplified only. The anti-phasic ones are not only increased, yet also result in a higher x_2 amplitude compared to x_1.

The presented 2-DoF mass spring system served as an introduction of the theory. However, it does not represent the SEA system considered in this thesis. Although the motor mass of the SEA unit is usually small in comparison to the link-side and thus neglected, we here focus on a scenario where the magnitude of motor and link inertia is in a comparable range. In this case, we can compare the two presented

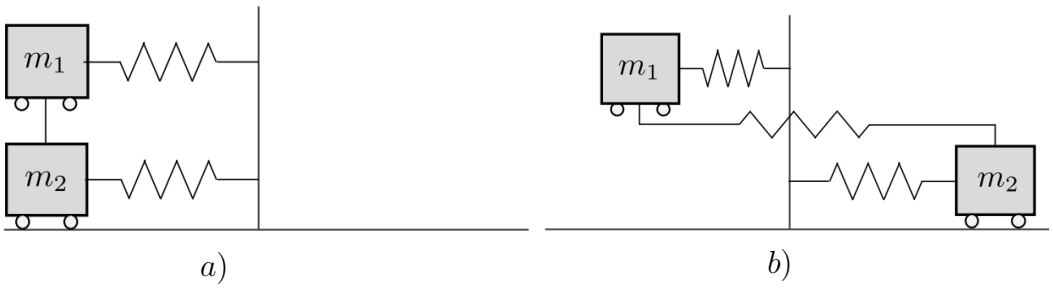

Figure 2.10: Illustration of a linear system with two degrees of freedom with a) in-phase and b) anti-phase normal mode, adapted from [39].

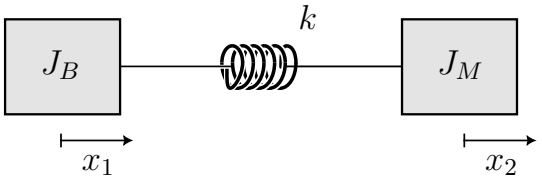

Figure 2.11: Physical schematic of an SEA system for frequency analysis with two outer masses J_B and J_M, connected by a spring with stiffness k.

masses m_1 and m_2 with the motor inertia J_B and the link inertia J_M shown in Figure 2.5, respectively. Similar to the linear mode example in Section 2.3, we now consider a one-spring-two-mass system receiving the depicted schematic in Figure 2.11.

The Langragian differential equations can be computed with

$$L \;=\; [T] \;-\; [V] \;=\; \left[\frac{1}{2}J_B\dot{x_1}^2 + \frac{1}{2}J_M\dot{x_2}^2\right] - \left[\frac{1}{2}k(x_2 - x_1)^2\right] \tag{2.22}$$

where the coordinates of the masses are denoted with x_1 and x_2 respectively. Solving the Euler-Lagrange $\frac{d}{dt}\left(\frac{\partial L}{\partial \dot{x}_i}\right) = \frac{\partial L}{\partial x_i}$, the definition of the differential equations in state space yields

$$\underbrace{\begin{bmatrix} J_B & 0 \\ 0 & J_M \end{bmatrix}}_{M} \begin{bmatrix} \ddot{x}_1 \\ \ddot{x}_2 \end{bmatrix} + \underbrace{k \begin{bmatrix} 1 & -1 \\ -1 & 1 \end{bmatrix}}_{\Gamma} \begin{bmatrix} x_1 \\ x_2 \end{bmatrix} = \begin{bmatrix} 0 \\ 0 \end{bmatrix} \tag{2.23}$$

where M and Γ represent the inertia- and stiffness property matrices, respec-

tively. Note that this is a simplified model, friction, stiffness, damping, motor-side impedance and various other influences are being neglected in order to get a first glimpse on the harmonic oscillation of the system. The calculation of the eigenvector can be done via solving the characteristic equation (2.18) and therefore leading to

$$\Lambda = k \begin{bmatrix} J_B^{-1} & -J_B^{-1} \\ -J_M^{-1} & J_M^{-1} \end{bmatrix} \rightarrow \lambda = \begin{bmatrix} 0 \\ k(J_B + J_M)(J_B J_M)^{-1} \end{bmatrix} \tag{2.24}$$

Since the first eigenvalue is 0, the 2-DoF system can only oscillate with the effective mass. The respective eigenfrequency is according to

$$\omega_{2D} = \sqrt{\lambda_2} = \frac{1}{2\,\pi}\sqrt{\frac{k(J_B + J_M)}{J_B J_M}} \tag{2.25}$$

The eigenfrequency of an SEA system, where the motor mass is also in motion, would thus be expected to be ω_{2D}. In addition to this, we also regard the case in which the motor is held relatively static, mainly holding J_B and only moving little, as this is a widely spread strategy in actuation. To evaluate the resonance frequency, when the motor position θ is fixed, the Langragian system can be reduced such that J_M is connected to a fixed wall, i.e., only 1-DoF remaining. The resulting differential equation can be computed as $J_M\ddot{x} + kx = 0$. For this case, the 1-DoF eigenfrequency becomes

$$\omega_{1D} = \frac{1}{2\,\pi}\sqrt{\frac{k}{J_M}} \tag{2.26}$$

In summary, we derived two relevant eigenfrequencies (ω_{1D} and ω_{2D}) for the investigated SEA system. The 1D principle considers the motor as mainly static, only moving little to excite the link-side dynamics. As this is in contrast to the 2D case, where a control approach with large motor mass movement is chosen in order to achieve the link oscillation. We will revisit the eigenfrequencies in Chapter 3 and Chapter 4.

2.4 Inertia Shaping

In the previous section, we discussed normal modes of a linear system $\in \mathbb{R}^{2x2}$. As seen from the analytical derivation, the trajectories and frequencies of these modes

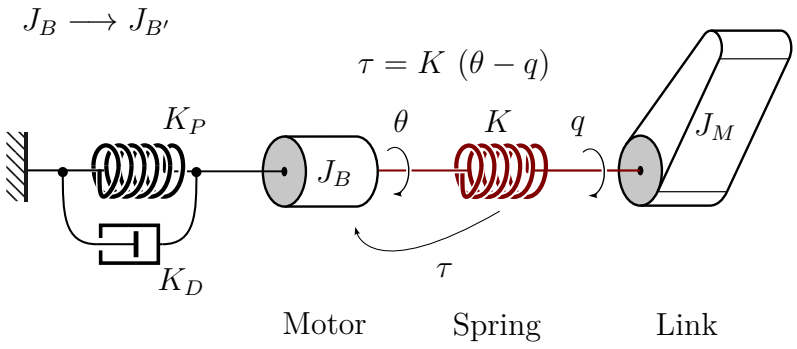

Figure 2.12: Exemplary depiction of a PD-controlled SEA with spring torque feedback τ for inertia shaping of the motor.

depend on the stiffnesses in the system and the ratio of the masses. Although it is not possible to change these parameters physically on a hardware system, control concepts can be used to virtually alter them. One such concept is through inertia shaping [40] [41], where the behavior of the system can be shaped by adding a feedback of the attached spring torque. The motor inertia remains in its physical characteristics unchanged, but the motor torque tries to match a specific target requirement in order to compensate its weight property.
This section will cover the control of SEAs in terms of shaping the motor inertia based on the research from [40].

Consider the earlier proposed system with its generalized equations of motion (2.2) and (2.3) and Figure 2.12 with an exemplary schematic of a PD-controlled SEA. Let us assume a scenario where link-side force is externally aplicated and the motor inertia J_B is much higher compared to the link inertia J_M. Hence, the motor position θ would result in less movement. Inserting a negative feedback of the joint torque τ enables to scale the motor inertia in such a way that the system is able to follow a desired dynamical behaviour.

Under consideration of [40] and the earlier shown SEA dynamics in equation (2.5), the feedback with insertion of a new motor inertia $J_{B'}$ can be expressed as

$$u = J_B \; J_{B'}^{-1} \; u' \; + \; (\mathbb{I} \; - \; J_B \; J_{B'}^{-1}) \; \tau \tag{2.27}$$

where u' serves as the new control input for the equations of motion.

This method allows us to successfully alter the inertia of systems in order to achieve certain behaviours in terms of dynamics or trajectory planning. Thus resulting in advantages such as high accracy, exceptional tracking performance and larger design freedom, e.g., regarding pole placement, controller design [41]. We will exploit the benefits of this control approach in Chapter 5, where a specific hardware experiment is conducted in order to investigate characteristics regarding the 2D control. The analyzed results will provide an overview in comparison to different physical motor inertia properties in simulation.

3 Control Theory Approaches

The objective of the following chapter is the introduction of the controllers applied in this thesis. As initially stated, the goal is to derive and implement control methods that excite and stabilize intrinsic oscillations in a robotic system with one SEA-joint. For this purpose, three control approaches have been investigated, either solely exciting the link-side dynamics or exciting the link-side in a 2-DoF spring-mass manner, by adding the motor-side motion. Specifically inspired by the mode theory, the question arose whether benefits can be gained from exploiting the motor inertia, instead of link inertia only, which intuitively seems useful for systems where the motor mass is higher than the link mass. The tested control approaches were compared to the state-of-art ESPi control, introduced in the previous Chapter 2. Each of the investigated control strategies and its derivation are presented in the following.

3.1 $1M-T(racking)$: One-Dimensional Oscillatory Motion

The first approach considers the excitation of the link-side dynamics only, by applying classical link-side resonance excitation of 1D SEA systems and following a tracking control design (1 Mass-Tracking ($1M$-T)). The goal of $1M$-T is to achieve oscillatory movement of the link by regarding the motor-side as an (almost) static wall and achieve this behaviour by means of a tracking controller. As this requires declaration of a motor position control error $\tilde{\theta} = \theta - \theta_d$, which will be introduced later, see Figure 3.1.
Since the motor-side desired behaviour is now defined, we can start implementing the link-side concept. Figure 3.2 shows the desired control for the link behaviour.

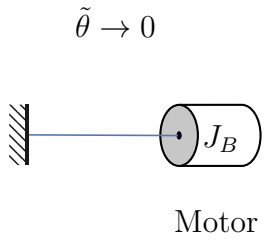

Figure 3.1: Graphical representation of the desired motor-side behaviour of the $1M$-T control design.

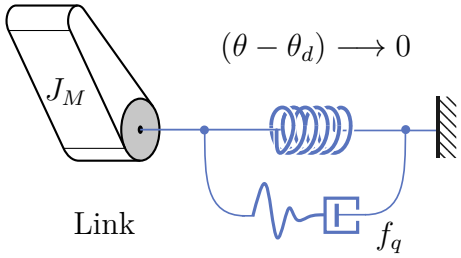

Figure 3.2: Graphical representation of the desired link-side behaviour of the $1M$-T control design.

The introduction of a new control symbol, located below the spring, depicts the desired excitation. We propose excitation of the link by regulating the energy to the system with $\gamma(q, \dot{q})$. Here, γ serves as a state dependent variable of link-position and -velocity, which is realized over a real-time energy feedback. Via this approach, we can prevent infinite excitation and ensure stability. The state dependency and its energy feedback will be explained shortly hereafter. For now, we present the link excitation with the expression

$$f_q \;=\; \gamma(q, \dot{q})\; \dot{q} \tag{3.1}$$

Consider Figure 3.3, where the $1M$-T control design is depicted. The derivative part $K_D\; \dot{\theta}$ is damping proportionally to motor velocity and $K_P\; \tilde{\theta}$ is constraining the motor movement via the control error $\tilde{\theta}$, see (3.4). We can define the desired

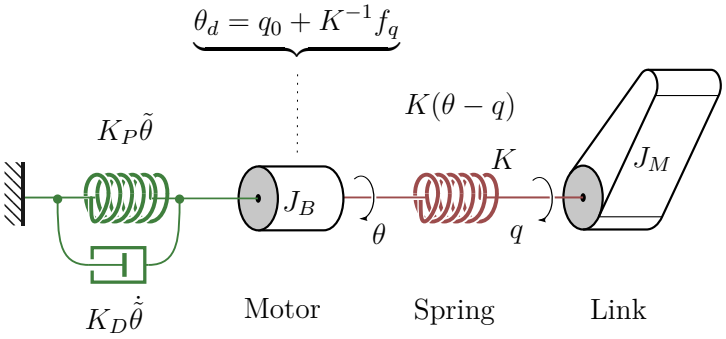

Figure 3.3: Graphical representation of the $1M$-T control design with link-side excitation and stiff actuated motor-side impedance.

link dynamic behaviour in (3.2), which directly corresponds to the mass dynamics law with the relation of the original- and desired-system. Notice that, q_0 represents the equilibrium position variable of the desired link motion, q and θ the link- and motor-position variables, respectively. For simplicity the energy input along the link velocity ($\gamma(q, \dot{q})\ \dot{q}$) will be replaced with f_q in the following.

$$J_M\ \ddot{q}\ =\ K\ (q_0 - q) + f_q \tag{3.2}$$

By equating the original system (2.4) with the desired one (3.2), we solve for θ and receive the desired motor position θ_d for the proposed control method of link-side excitation. Thus, being provided with a transformation equation for the computation of a valid control law

$$\theta\ =\ \theta_d\ =\ q_0 + K^{-1}\ f_q \tag{3.3}$$

It is essential to point out that the excitation in this approach is mainly achieved through stiff actuation of the motor, with the introduction of the following motor position control error

$$\tilde{\theta}\ =\ \theta - \theta_d \tag{3.4}$$

Moreover, a definition of the desired motor-side behaviour is necessary to

assure stiff impedance and little motor movement with the following desired motor-dynamics law

$$\underbrace{J_B\ \ddot{\tilde{\theta}} + K_D\dot{\tilde{\theta}} + K_P\tilde{\theta}\ =\ 0}_{\text{desired behaviour}} \tag{3.5}$$

We choose $\tilde{\theta}$ to maintain $\tilde{\theta} \to 0$ for $t \to \infty$ and equate the dynamics to 0. By fulfilling the proposal from equation (3.5) with correspondence to the original motor dynamics ($J_B\ddot{\theta} + K(\theta - q) = u$), from the earlier presented SEA-system in Section 2.2, we can derive the final control law

$$u\ =\ J_B\ \ddot{\theta}_d + K\ (\theta - q) - K_D\ \dot{\tilde{\theta}} - K_P\ \tilde{\theta} \tag{3.6}$$

The proof of concept is followed by equating the original system properties (2.5) with the final control law (3.6), thus receiving the desired behaviour in (3.5).

As already indicated, taking a closer look at term (3.1) reveals instability through constantly adding energy with the state dependent factor γ. To overcome this difficulty, we present an excitation control method, by calculating the energy in the system in order to limitate the enery delivery. Hence, the one dimensional energy of the link is calculated via

$$E_{msr-1D} = \frac{1}{2}\ K\ (\theta - q)^2 + \frac{1}{2}\ J_M\ \dot{q}^2 \tag{3.7}$$

This can now be compared to the desired energy, what directly yields to a new calculation of the excitation

$$f_{q-1D} = \underbrace{(E_d - E_{msr-1D})}_{\gamma(q,\dot{q})}\ \dot{q} \tag{3.8}$$

where E_d represents a constant and E_{msr-1D} the energy feedback calculation. Consider the earlier desired link behaviour (3.2), where $\gamma(q, \dot{q})$ promptly reveals two dimensional state dependency for our desired eigenmode. As q and $\dot{q}$ pass the equilibrium, the state of energy input switches accordingly in order to excite the link into both directions of movement.

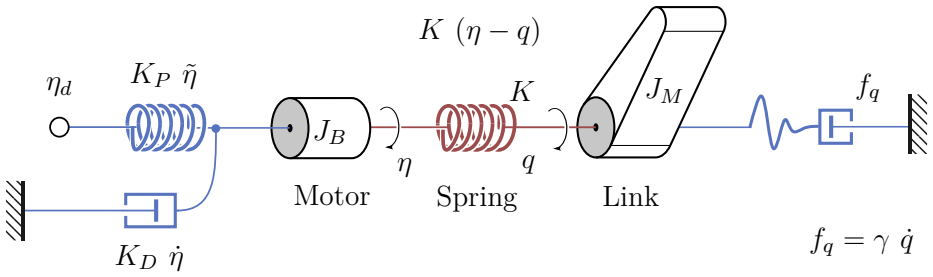

Figure 3.4: Graphical representation of the $1M - E(S\pi)$ control design with link-side excitation, desired virtual motor coordinate and motor-side behaviour.

By computation of the required derivatives of equation (3.7) for control, $1M$-T successfully achieves intrinsic oscillatory frequency movement of the link via motor-side tracking control.

3.2 $1M - E(S\pi)$ based Periodic Excitation

Another approach to exploit the dynamics in our presented SEA-system, is based on the earlier presented ESPi controller of Section 2.2. Instead of locking the motor position via tracking control of ($1M$-T), the goal of 1 Mass $ES\pi$-based Periodic Excitation ($1M - E$) is to guarantee desired behaviour of motor dynamics with the introduction of a desired virtual motor coordinate η_d. Moreover, η_d enables the user to control the equilibrium coordinate of the oscillatory motion on the motor-side, see Figure 3.4.

Consider the presented system from Figure 3.4, we can start deducing the desired mass dynamics for the link and motor with respect to $\tilde{\eta} = \eta - \eta_d$, yielding therefore

$$J_M\ \ddot{q} = K\ (\eta - q) + f_q\ , \tag{3.9}$$

$$0 = J_B\ddot{\eta} + K(\eta - q) + K_D\dot{\eta} + K_P(\eta - \eta_d)\ . \tag{3.10}$$

η represents the virtual motor coordinate of the desired control, $K_D\dot{\eta}$ and

$K_P(\eta - \eta_d)$ the motor-side impedance, respectively. Equation (3.9) directly leads to the characteristic link mass equation of the original and desired link-side behaviour with

$$\underbrace{K(\theta - q)}_{\text{original}} = \underbrace{K(\eta - q) + f_q}_{\text{desired}} \tag{3.11}$$

and solving this for η in order to get the tranformation equation

$$\eta \;=\; \theta \;-\; K^{-1}\; f_q \tag{3.12}$$

In addition, we can equate the motor-mass dynamics (see (3.10) and (2.5)) by solving

$$J_B\ddot{\theta} \; + K\theta \; - u \;=\; J_B\ddot{\eta} + K\eta + K_D\dot{\eta} + K_P(\eta - \eta_d) \tag{3.13}$$

Finding the derivatives of the transformation equation and inserting them into (3.13), a solution for the required control law is found

$$u = K^{-1}\; J_B\; \ddot{f}_q + f_q + K_P\; (K^{-1} f_q - \theta + \eta_d) + K_D\; (K^{-1}\dot{f}_q - \dot{\theta}) \tag{3.14}$$

$1M - E$ enables us to choose a desired motor position, also letting us control motor-side impedance directly via proportional and derivative parameters. Similar to the ESPi, the $1M - E$ preserves the elastic structure of the plant. As this is a vital point for reaching intrinsic oscillatory frequency of the link. The excitation is solved via a one dimensional energy solution with two dimensional state dependency $\gamma(q, \dot{q})$, as presented in Section 3.1 for the $1M$-T.

3.3 $2M - V(elocity)$: Two-Dimensional Oscillatory Motion

The previous presented control approaches are based on the principle of considering the resonance frequency of the link mass only. However, based on the idea that it might be beneficial to exploit the dynamics of the motor inertia in some cases, another control approach is investigated. In this approach, the SEA is regarded as

a two mass system, similar to the depicted figure in Section 2.3 (Figure 2.9). The goal is to derive a strategy such that the inertia of both motor and link can be exploited, which is suspected to be especially useful when the motor inertia J_B is (much) bigger than the link-side inertia. This design preference will be referred to as the 2 Mass-Velocity Excitation ($2M-V$), based on [42].

Instead of demanding stiff motor-side actuation for the excitation, we rather seek to expand the movement of the motor mass in order to evaluate the efficiency regarding a potential exploitation of the motor inertia. The implementation of an *accelerator* f_q is realized via an excitation of the system along the link velocity $\dot{q}$.

Derived from the presented SEA in Figure 2.5, we can compute a valid control law

$$u \;=\; f_q \;=\; \gamma(q, \dot{q}, \theta, \dot{\theta})\; \dot{q} \tag{3.15}$$

Similar to the energy management of the $1M$-T and $1M-E$, we focus on the computation of the total energy of the system for the $2M-V$, instead of focusing on the link inertia only, since both motor- and link-inertia are being excited.

Thereby, letting us calculate the energy of the system

$$E_{msr-2D} = E_{tot} = \underbrace{\frac{1}{2}\; K\; (\theta - q)^2}_{\textit{potential}\text{ part}} + \underbrace{\frac{1}{2}\; J_M\; \dot{q}^2 + \frac{1}{2}\; J_B\; \dot{\theta}^2}_{\textit{kinetic}\text{ part}} \tag{3.16}$$

which at the same time represents the total energy E_{tot} of the given SEA system.

Note that here, state dependency for excitation is four dimensional $\gamma(q, \dot{q}, \theta, \dot{\theta})$[1]. Likewise in the previous control concepts, we compute an energy error for reaching a desired level with

$$\tilde{E} = E_{des} - E_{msr-2D} \tag{3.17}$$

where E_{des} is representing the desired energy for control.

[1] see Section 3.1 for further information

By calculating f_q, under the assumption of $\tilde{E} \rightarrow \gamma(q, \dot{q}, \theta, \dot{\theta})$, we can successfully prevent infinite oscillation of the link.

As one may intervene regarding the stability of the presented desired dynamics, we must adjust the proposed control law in order to prevent the system from position drift.
Therefore, we tend to realize control via decoupling the nature of the given SEA into two one-body problems for equations of motion in new coordinates. We introduce the calculation of the spring equilibrium point via

$$\phi = \theta - q \tag{3.18}$$

and the Center Of Mass (COM) position as a generalized coordinate of the system with total inertia J_{MB} ($= J_M + J_B$).

$$\xi_{com} = \frac{J_M\, q + J_B\, \theta}{J_{MB}} \tag{3.19}$$

The kinetic energy of the excitation (of both motor- and link-inertia) [42] is given by the new coordinates with

$$E_{kin} = \frac{1}{2}\, J_{MB}\, \xi_{com}^2 + \frac{1}{2}\, (\Psi\, \dot{\phi}^2 + K\, \phi^2) \tag{3.20}$$

where the combined inertia J_{MB} swings with the velocity of the COM position and Ψ suits as the reduced mass with relative position movement, fulfilling

$$\Psi \equiv \frac{J_M\, J_B}{J_{MB}} < min(J_M, J_B) \tag{3.21}$$

This derivation enables us rewriting the equations of motion for this approach

$$J_{MB}\, \ddot{\xi}_{com} = u\ , \tag{3.22}$$

$$\Psi\, \dot{\phi} + K\, \phi = \frac{J_M}{J_{MB}}\, u\ . \tag{3.23}$$

For control of the presented ξ_{com} signal, we consider Proportional Integral Derivative Control (PID) with respect to the equilibrium position q_0 of the system, resulting in the control error $\tilde{\xi}_{com} = q_0 - \xi_{com}$. Figure 3.5 depicts the desired

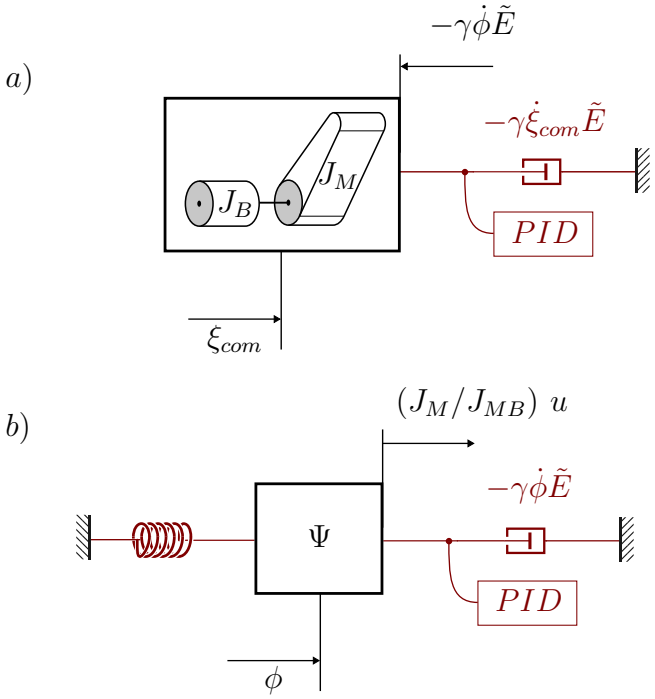

Figure 3.5: Graphical representation of the desired excitation control with coordinate transformation for the $2M-V(elocity)$: a) showing the first body problem with control of the combined mass J_{MB} and b) the second body problem with the proposed control of the reduced mass Ψ.

behaviour for the $2M-V$ approach. The SEA is transformed into a two-body problem, according to the previous denoted equations of motion (3.22) and (3.23). Goal is to excite the total mass J_{MB} in Figure 3.5 a), while bottom figure b) shows the control of the reduced mass Ψ oscillating about a fixed center. Here, the velocity is based on the relative position. We can introduce the required control law with a stable equilibrium point and oscillatory movement with

$$u \;=\; \tilde{\xi}_{com} \;-\; \gamma(q,\dot{q},\theta,\dot{\theta})\;\dot{\phi}\;\tilde{E} \tag{3.24}$$

The $2M-V$ successfully manages to excite both motor- and link-mass, thus reaching the combined intrinsic oscillatory frequency (2.25) of the system. This directly leads to an increase of the motor velocity $\dot{\theta}$ and therefore opens a path for potential inertia exploitation. Based on this novelty, we want to examine the field of efficiency increase in the following.

4 Validation

In order to validate the presented controllers and investigate the benefits of each, simulation and hardware experiments were carried out, which are presented in the following. For these experiments a single joint SEA based robot (SOFTY [43]) is used, on which the three different control approaches introduced in the previous chapter are implemented. We first give an overview of the system and carried out experiments to characterize the dynamics behavior of the hardware. Characteristics regarding eigendynamics are analyzed and following we compare the investigated control approaches, in simulation and in actual hardware experiments.

4.1 Elastic Robot Testbed SOFTY

The elastic robot testbed SEA-based robot with one link (SOFTY) (Figure 4.1) is used in this thesis to compare the derived control approaches. The link is attached to a belt drive, which incorporates two parallel springs to realize the elasiticity of the system, amounting to a linear stiffness value of 362 N/m. The inertia of the motor mass is 0.598 $kg\,m^2$, while the center of mass of the link is manipulated such that the link's intertia is 1 $kg\,m^2$. The controller sample time equals 0.000333 s. All relevant parameter values are summarized in Table 4.1.

As stated in Chapter 2, no gravitational effects need to be reconsidered due to horizontal movements only. The used actuator is a single joint of a DLR Light Weight Robot (DLR-LWR), where a Brushless DC Motor (BLDC) motor is coupled to a harmonic drive gear, mentioned in the following as Electro-Magnetic Actuator (EMA). Motor positions and velocities are recorded through the internal sensors of the EMA system, and an additional sensor on the link-side allows the tracking of

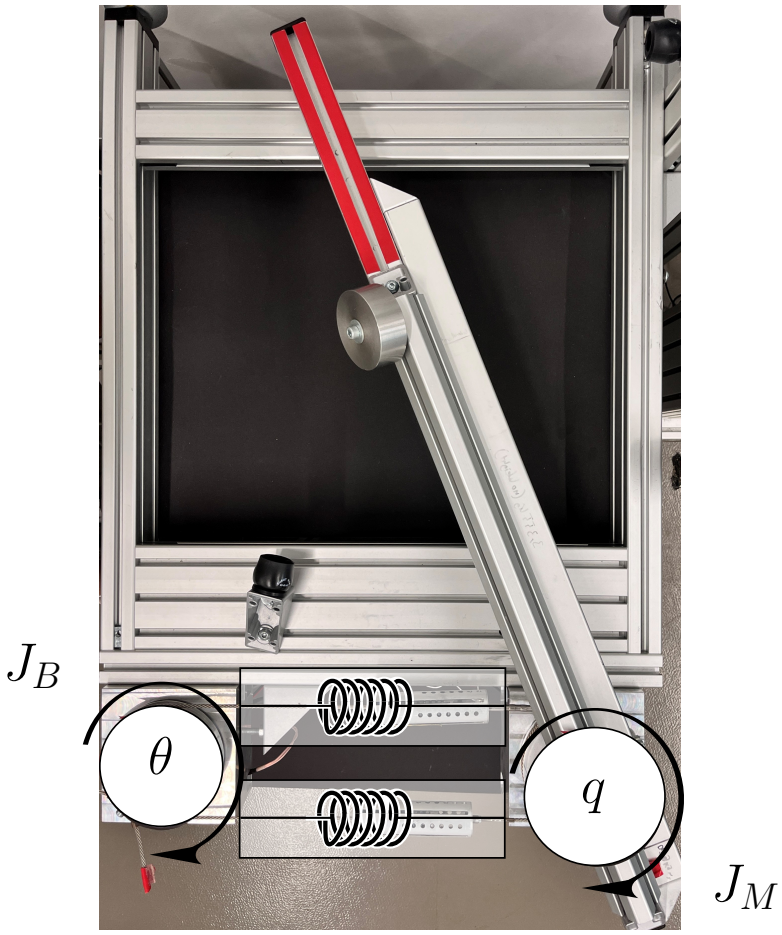

Figure 4.1: SEA-based robot SOFTY with horizontal movement of the motor-position θ and link-position q, the inertia of the motor- and link-side are denoted J_B and J_M, respectively, and the connecting spring has the stiffness K.

Table 4.1: Main parameters of SOFTY.

Parameters	Values	Unit
Motor Inertia (J_B)	0.598	$\mathrm{kg\,m^2}$
Stiffness of Mechanical Spring (K)	362	N/m
Link Inertia (J_M)	1	$\mathrm{kg\,m^2}$
Physical Damping (D)	1.7209	N s/m

Table 4.2: Theoretical values of the eigenfrequency of two systems with their corresponding control methods, ω_{1D} representing a one-mass-spring system connected to a wall and ω_{2D} a two-mass-spring system as depicted in Figure 2.11.

Theoretical Resonance Frequency	Values	Unit
ω_{1D} of Link ($1M$-T & $1M-E$)	3.028	Hz
ω_{2D} of Link and Motor ($2M-V$)	4.950	Hz

the respective link measurements. Thus, the spring torque τ according to (2.1) can be calculated in the control loop. To additionally measure the motor current as a parameter to quantify the expended physical work, a EL3681 EtherCAT sensor was added. The current to the motor is measured at 50 Hz sampling frequency. Since the testbed is running on 3 kHz the behaviour of the current signal is not analyzed in detail, instead the mean value over the complete measurement is analyzed for each control approach. The robot-communication is based on real-time computing over the MATLAB® Simulink Coder™. Therefore, following simulations and hardware implementations are realized via Simulink.

The main objective of this thesis is to investigate different control strategies that make use of the intrinsic dynamics of a system and compare whether or not it has an advantage to also make use of the motor dynamics. In order to validate whether the intrinsic dynamics of the hardware are supported, the SOFTY system is first characterized and the normal modes analytically derived. When assuming the motor mass to act as a wall, such that only the link dynamics are excited, the eigenfrequency is defined by (2.26) (with $k = K$). This results in an eigenfrequency of 3.028 Hz. When also trying to exploit the motor mass, the system becomes a 2-DoF sping system (explained in Chapter 2) and the eigenfrequency is defined by (2.25). The eigenfrequency of the 2D system results in 4.950 Hz. Both values with the respective relevance for the investigated controller are summarized in Table 4.2. While it is expected that the $1M$-T and $1M-E$ approch will excite the 1D-eigenfrequency of the system, the $2M-V$ controller should result in an oscillation close to the 2D-eigenfrequency.

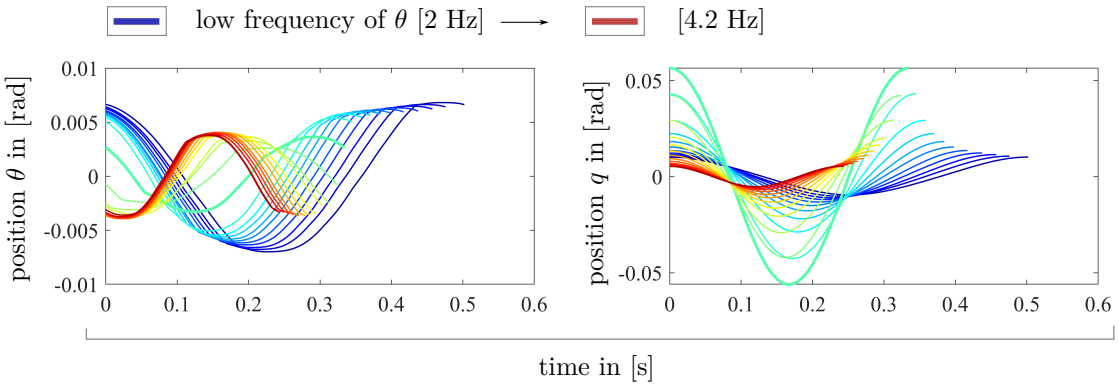

Figure 4.2: Normal mode characterization of SOFTY: frequency sweep of sinusoidal motor position θ trajectory command (*left*) and the resulting link position q (*right*) with highest output colored in turquoise.

For validation of those results, a frequency sweep was applied on the SOFTY hardware in motor position control mode. A sinusoidal trajectory for θ was commanded with a fixed amplitude of 0.01 rad with continuously increased frequencies from 2 Hz to 4.2 Hz in 0.1 Hz steps. The 2D harmonic frequency (of 4.7 Hz) could not be tested via this approach, due to physical property restrictions of the possible angles of q.
Figure 4.2 depicts the commanded motor position θ (*left*) and the resulting link position q (*right*). The peak amplitude is marked in turquoise, indeed arising at the expected eigenfrequency of 3 Hz for the case of neglectably little movement of the motor mass.

Figure 4.3 shows the visualization of a number of interesting values. In the following context, we will refer to W variables as physical work of transferred energy from one system to another and to E ($=$ *energy*) as the ability of a system to perform work. The most outer left panel depicts the system energy W_{sys} per period over the corresponding frequency value of θ. The system energy is defined to be the energy between the motor and spring of the SEA via

$$W_{sys} \;=\; \int P_{sys} \;=\; \int \dot{\theta}\, \tau \tag{4.1}$$

As seen in Figure 4.3, the energy delivered to the spring peaks in the SOFTY testbed at the expected eigenfrequency of 3 Hz, since the link mass is only excited little in comparison to the link. For the phase lag $\Delta\phi_{ang}$ between the motor and

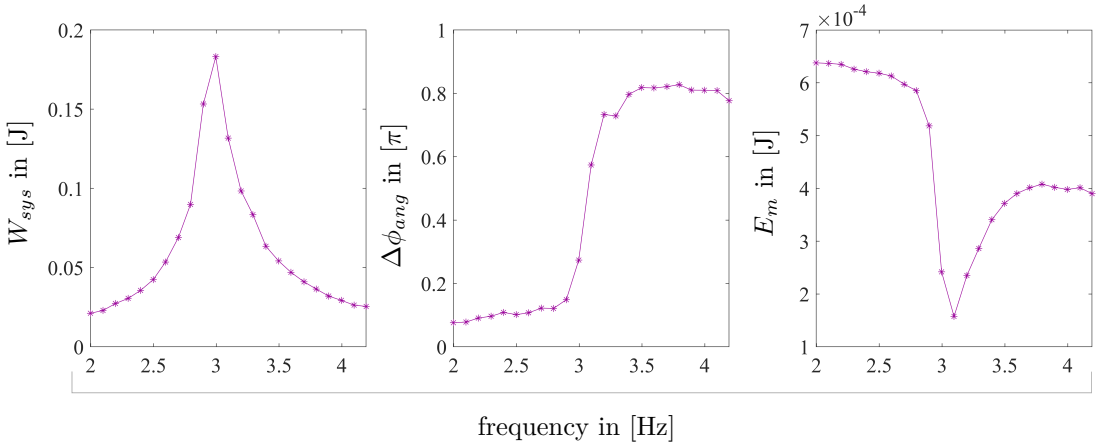

Figure 4.3: Normal mode characterization of SOFTY: calculation of system work W_{sys} per period (*left*), phase difference $\Delta\phi_{ang}$ (*middle*) between θ and q & motor energy E_m per period (*right*).

the link position, a flip can be observed when the eigenmode is hit. Initially moving in phase, the motor link starts to move increasingly in anti-phase above the eigenfrequency.

The kinematic motor energy (Figure 4.3 right) defined by

$$E_m \;=\; \frac{1}{2}\, J_B\, \dot{\theta}^2 \tag{4.2}$$

shows a minimum at the eigenfrequency resulting from the minimal movement of the motor for this value. Note that the total energy of the system is defined by the potential and kinetic energy parts of the SEA, denoted in (3.16), which we rename for analysis purpose in the following as $E_{tot} = E_{msr-2D}$.

Table 4.3 gives an overview of the measured and calculated values, which will be utilized throughout the analysis and for comparison of the various control approaches. We evaluate the measured current reaching the motor i_{msr} via electric power and energy consumption. Velocity and acceleration are being numerically differentiated. The commanded torque $u_{control}$ represents the torque commanded by the controller and is directly forwarded to the friction observer. The implemented friction observer [44] is based on joint torque measurement and depicted in Figure 4.4 as signal flow diagram. The general observer dynamics are defined by

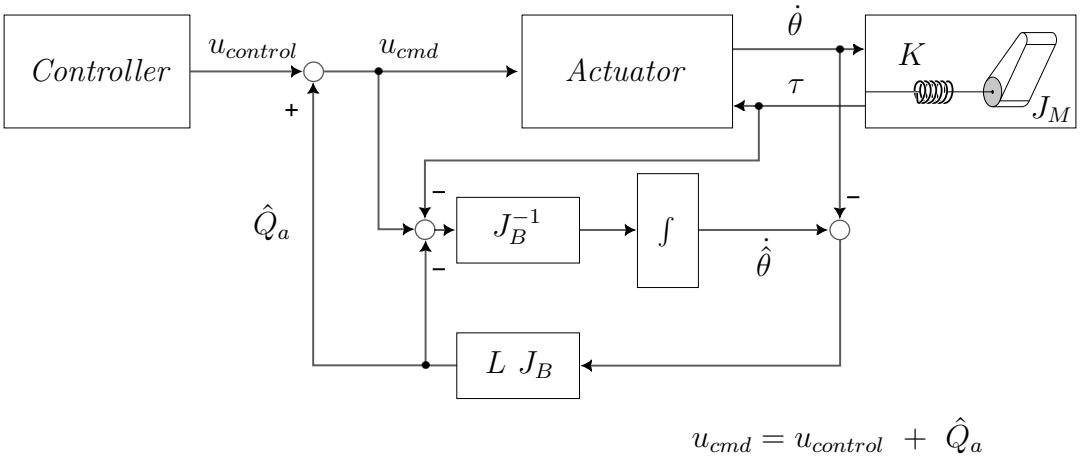

Figure 4.4: Signal flow diagram of the friction observer implementation in Simulink, with the friction estimation $\hat{Q}_a$, the observer feedback value $L > 0$ and the estimation error of the motor velocity $\dot{\tilde{\theta}} = \dot{\hat{\theta}} - \dot{\theta}$, adapted from [44].

$$u_{cmd} = \ddot{\hat{\theta}} J_B + \tau + \underbrace{L\ J_B\ (\dot{\hat{\theta}} - \dot{\theta})}_{\hat{Q}_a} \tag{4.3}$$

where the estimation error of the motor velocity is $\dot{\tilde{\theta}} = \dot{\hat{\theta}} - \dot{\theta}$ and $\hat{Q}_a$ the friction estimation.

Note that the final processed signal to the actuator u_{cmd} has friction compensation included, whereas the generated torque of the controller $u_{control}$ does not, since $u_{cmd} = u_{control} + \hat{Q}_a$. This will be revisited as part of the following analysis about the controller comparison.

Table 4.3: Overview of experiment signals for analysis and comparison of the control approaches.

Type	Symbol	Formula *	Unit
Measured Current	i_{msr}		[mA]
Electric Power	P_{el}	$P_{el} = i_{msr}\ 48V$	[W]
Work of Motor	W_{el}	$\int\ P_{el}$	[Ws]
Power of System	P_{sys}	$\dot{\theta}\ \tau$	[W]
Work of System	W_{sys}	$\int\ P_{sys}$	[Ws]
Commanded Torque	$u_{control}$		[Nm]
Commanded Torque Peak	$\hat{u}_{control}$		[Nm]
Friction Observer Commanded Torque	u_{cmd}		[Nm]
Fr. Obs. Commanded Torque Peak	$\hat{u}_{cmd}$		[Nm]
Amplitude of Motor/ Link	$\hat{\theta}/\hat{q}$		[rad]
Amplitude Difference	$\Delta\hat{a}$	$\hat{q} - \hat{\theta}$	[rad]
Rotor Velocity	$\dot{\theta}$		[rad/s]
Rotor Acceleration	$\ddot{\theta}$		[rad/s^2]
Link Velocity	$\dot{q}$		[rad/s]
Link Acceleration	$\ddot{q}$		[rad/s^2]
Frequency of Link	ω_q	$1/T$	[Hz]
Phase Difference	$\Delta\Phi_{ang}$		[π]
Friction Evaluation	μ_{obs}	$\int \hat{Q}_a\ \dot{\theta}$	[Ws]
Desired Link Position for ESPi	q_d		[rad]
Number of Periods in Measurement	n_p		

* measured and numerically calculated signals are left out

4.2 Experimental Procedure

In order to investigate the behavior and resulting performance of the system for the different derived control strategies introduced in Chapter 3, they were implemented in the SOFTY hardware testbed within the existing Simulink control architecture. Since we expect the different controllers to excite different frequencies, we had to define a specific control goal for comparison, which, for the time being, was not dependent on the frequency. This goal was inspired by a "pick-and-place task", as could be needed in an industrial setting. Thus, we defined a motion range of $\hat{q} = 0.05\ rad$ for the link-side trajectory with a control goal of $\approx 5\%\ \tilde{\hat{q}}$ deviation and tuned the control parameters for each strategy accordingly. As mentioned, for this initial investigation of the controller perfomance in context of this thesis, we regard the resulting frequency of the system of neglectable importance, but are aware that it needs to be considered for a real application. Additionally the amount of physical work per timestep or per period of a mean steady state period is calculated for the friction estimation torque $(\int \hat{Q}_a \dot{\theta})/\Delta t$, in order to quantify the inbound friction.

In order to not only compare the introduced control strategies with each other, but also quantify them with regard to existing state-of-the-art methods to carry out oscillatory motions with a compliant system, additionally ESPi controllers (explained in Chapter 2) were implemented in the SOFTY testbed. The ESPi, control parameters were tuned such that the same amplitude was reached as defined for the control goal. The frequency was varied to be 0.3, 3 and 4.7 Hz to draw a comparison in control, for which the ESPi was developed, as well as an approach where the identified eigenfrequencies of the 1D- and 2D-system were hit. Here, we require q_d, as the desired link position of the ESPi control for sinusoidal trajectory input (see Chapter 3).
To record the data analyzed for the comparison of the controllers, the system was initialized with each controller tuned to achieve the given amplitude task. The transient time was not included in the investigation and comparison. Once the system had reached a stable amplitude, the system measurements were recorded. From these recordings, we averaged 25 periods and calculated the metrics presented in Table 4.3.

The same procedure was applied for simulation experiments of the system to take into consideration the system under ideal conditions with no apparent friction.

4.3 Experimental Results

In the following, the results of the simulation and hardware experiments to compare the applied control approaches will be presented. Table 4.4 gives an overview of characteristic values in order to identify the control behaviour with the desired pick-and-place amplitude. Figure 4.5 shows the measurement results of motor position signals θ and link position q. The transient time is not specifically analyzed in the scope of this thesis, it is shown for the simulation to provide quantitative additional information, which could be analyzed in further studies.

As expected, Figure 4.5 shows that for the 1M controllers, the motor only moved marginally leading to a high amplitude difference $\Delta\hat{a}$ between the motor position and the link position. In line with the theory, the $2M-V$ approach additionally excited the mass of the motor and showed anti-phasic movement. Comparing the simulation and the hardware results for the $1M$-T controller (Figure 4.5, *top*), indicated that the motor amplitude is slightly higher in the hardware than computed in the simulation, which is caused by the required friction compensation. This also corresponds to the desired behaviour where stiff control of the motor J_B with relatively high K_D and K_P was chosen. A similar pattern can be observed with $1M-E$ (Figure 4.5, *middle*), where the amplitude of θ is slightly larger than for the $1M$-T, but still comparatively small with respect to the link-side motion. The reason behind this is that impedance of $1M-E$ is chosen to be less stiff and the control approach preserves the elasticity of the plant (see Chapter 3).

The previous theoretical calculation of the 1D oscillation frequency ω_{1D} of 3 Hz corresponds well to the simulated- and hardware-tested values ω_q.

For the $2M-V$ the observed oscillation frequency of the hardware is with $\omega_q \approx 4.7\ Hz$ slightly lower than compared to the theoretical ($\omega_{2D} \approx 4.950\ Hz$) and simulated ($\omega_q \approx 4.946\ Hz$) values. The reason for this reduced eigenfrequency most likely arises from losses and imperfections, causing more damping with higher velocities in the system.

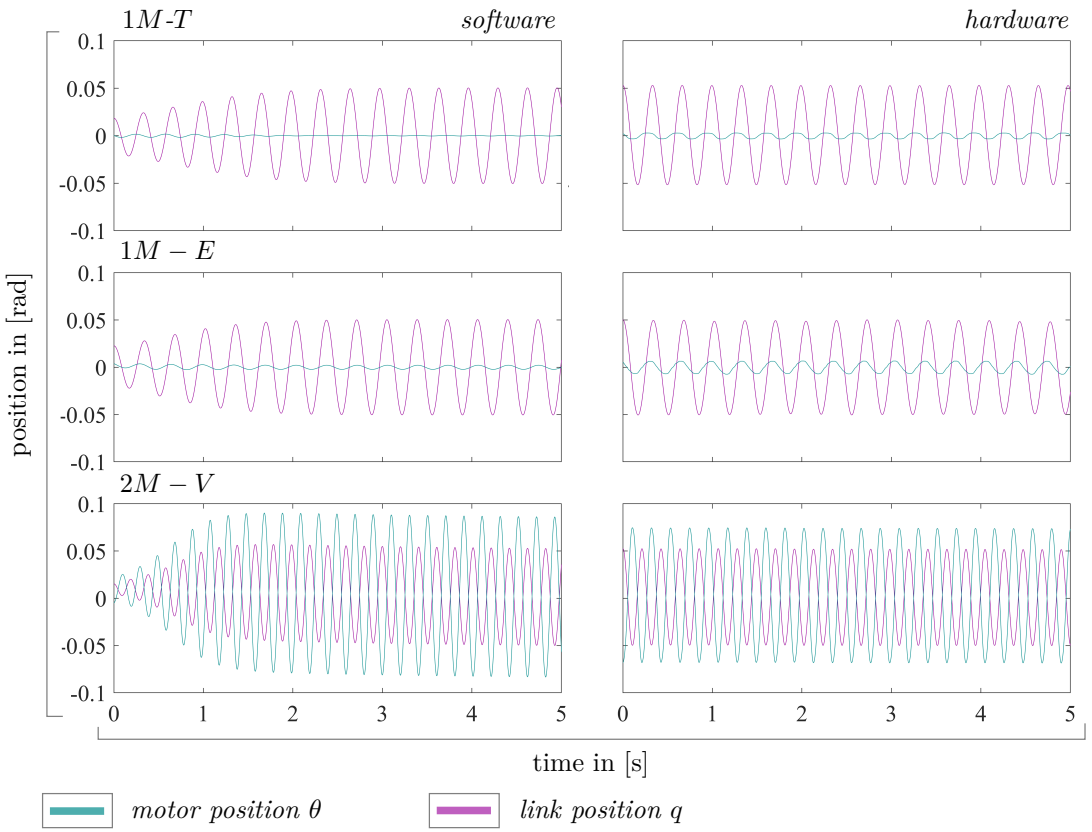

Figure 4.5: Measurement results of the three different control approaches for resonance excitation, θ and q as motor position and link position, respectively.

The descriptive values established that the controllers work as expected and excite the systems along the intended resonance frequencies. Since neither the oscillation frequency nor the specific motor amplitudes or torques were deemed as limiting factor. In the following the perfomance of the controllers will be compared with regards to the carried out physical work. This will only regard the needed control input to drive the already excited system oscillation and neglect the transient time period.

Figure 4.6 shows on the left hand side the commanded torques ($u_{control}$) to the hardware of the different controllers, as well as the friction compensated torques

Table 4.4: Overview of parameter values for analysis and comparison of simulation *vs.* hardware, as a first glimpse on the main behaviour of the presented controllers.

Controller	Parameter	Simulation	Hardware	Unit
$1M$-T	ω_q	3.029	3.014	Hz
	$\hat{q}$	0.049	0.053	rad
	$\Delta\hat{a}$	0.049	0.050	rad
	$\Delta\Phi_{ang}$	N/A	0.325	π
	$\dot{\theta}$ peaks	+0.007/-0.007	+0.084/-0.101	rad/s
$1M-E$	ω_q	2.960	2.938	Hz
	$\hat{q}$	0.050	0.049	rad
	$\Delta\hat{a}$	0.048	0.043	rad
	$\Delta\Phi_{ang}$	-0.024	0.237	π
	$\dot{\theta}$ peaks	+0.041/-0.041	+0.148/-0.138	rad/s
$2M-V$	ω_q	4.946	4.697	Hz
	$\hat{q}$	0.053	0.052	rad
	$\Delta\hat{a}$	-0.034	-0.022	rad
	$\Delta\Phi_{ang}$	0.995	0.977	π
	$\dot{\theta}$ peaks	+2.539/-2.565	+2.201/-2.191	rad/s

(u_{cmd}). On the right hand side, the system power is calculated, based on (4.1). Table 4.5 gives a brief overview of all metrics calculated for performance comparison. The comparison of these metrics reveals that the mean electric energy of the motor W_{el} per period has the highest value for the $2M-V$ controller. We can also tell from Table 4.5 that more energy is in the system when commanded by the $2M-V$ controller compared to the 1M-approaches, as indicated by the W_{sys} values. This is because $2M-V$ induces far more energy into the spring. Hence, by storing it, the required torque (for keeping the swing "alive") is drastically reduced (Figure 4.7).

Consider Figure 4.7, where 20 periods of the $u_{control}$ signal are depicted (in *black*) and τ_{msr} of a sensor is depicted over 20 periods in *grey*.

Taking a closer look at the torque measurements of the motions excited through

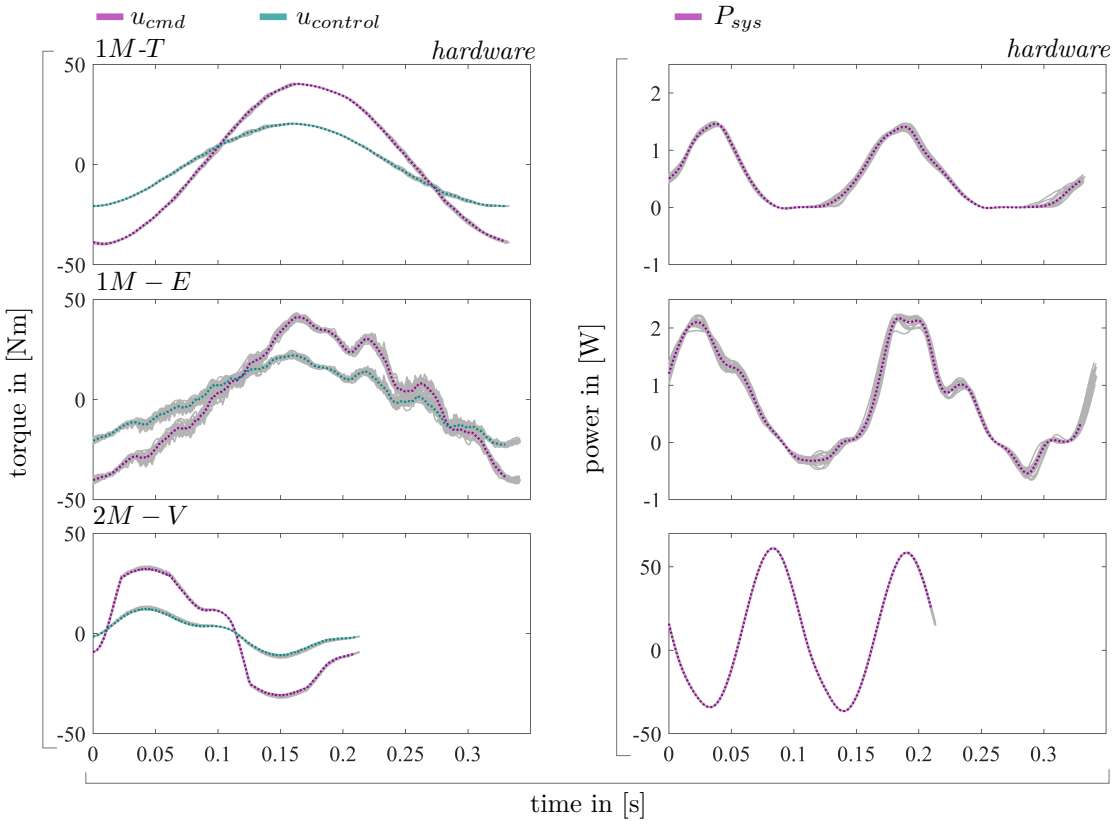

Figure 4.6: Commanded torque $u_{control}$, the commanded torque with friction observer u_{cmd} (*left*) and system power P_{sys} (*right*), with 20 periods (*grey*) and their mean signals (*colored*) respectively.

the different controllers shows an interesting observation. While for the $1M$-T and $1M - E$ controller the commanded torque u_{cmd} matches the torque that is arising in the system on the spring side, the same is not true for the $2M - V$ controlled system. Here, the system torque τ clearly deviates from the commanded torques. The reason is that for this particular static motor case of the 1M approaches, the motor inertia has no considerable effect on the system. This however, changes for the $2M - V$ approach where the motor greatly moves. For brevity, the dedicated plot of the $1M - E$ is not depicted, since it shows the same characteristics as $1M$-T.

Next, we will take a closer look at the amount of friction estimation per period, which is depicted in Figure 4.8. For a better evaluation, we choose to calculate $\mu_{obs} = \int \hat{Q}_a \, \dot{\theta}$. Although the general amount of friction that needs to be com-

Table 4.5: Overall performance of the three proposed control approaches with various parameters: W_{el}/T as mean electric energy to the motor per period, mean physical work of system W_{sys} per period (4.1), peak values for the in-torques $(\hat{u}_{control})$ & $(\hat{u}_{cmd})$, $\mu_{obs} = \int \hat{Q}_a \, \dot{\theta}$ as the amount of friction compensation energy per period and mean current to the motor $\varnothing \, i_{msr}$.

Controller	W_{el}/T	W_{sys}/T	$\hat{u}_{control}$	$\hat{u}_{cmd}$	μ_{obs}	$\varnothing \, i_{msr}$	ω_q
Unit	Ws	Ws	Nm	Nm	Ws	mA	Hz
$1M$-T	2.009	0.166	20.4	40.3	0.21	126	3.0
$1M-E$	2.096	0.279	22.3	41.4	0.36	128	2.9
$2M-V$	5.448	6.417	13.5	33.5	5.19	533	4.7

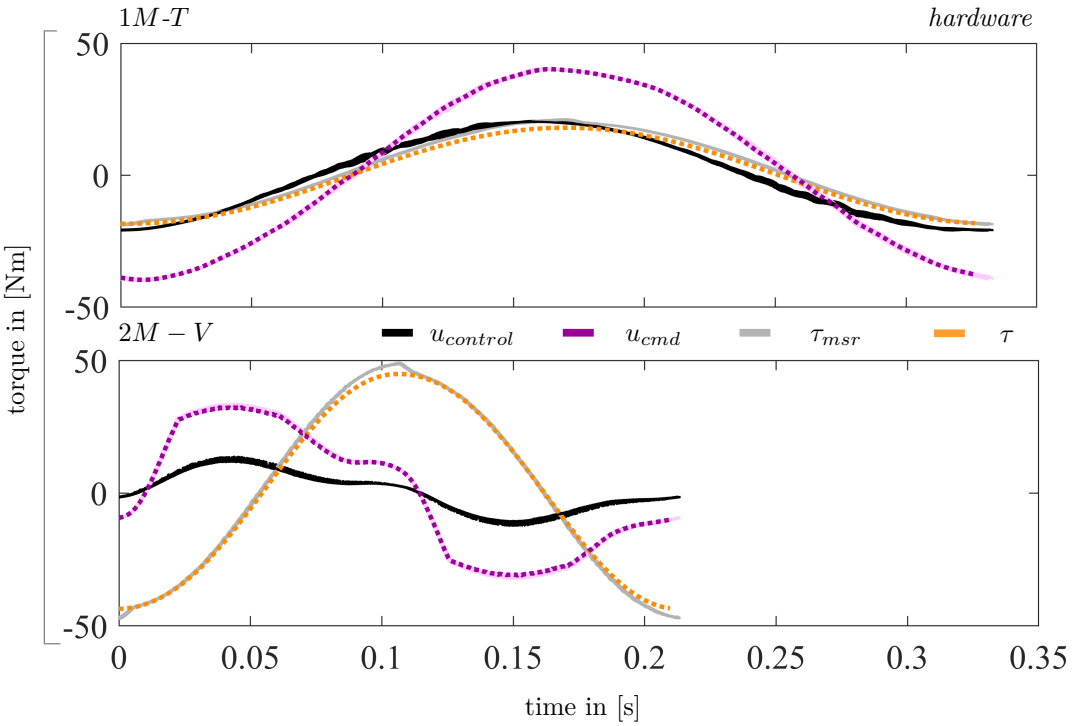

Figure 4.7: Energy difference between W_{el} and W_{sys} for the $2M-V$, spring torque τ, measured value by a sensor τ_{msr} and $u_{control}$ almost identical for $1M$-T, whereas in the $2M-V$ case not.

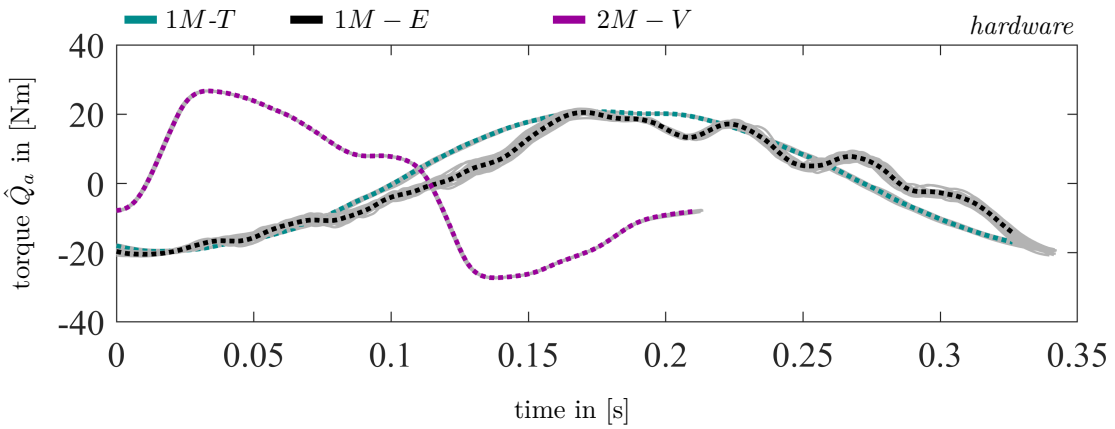

Figure 4.8: Friction compensation estimation $\hat{Q}_a$ for the 3 different control approaches with mean values (*colored*) and 20 periods (*grey*).

Table 4.6: Hardware measurements depicted per time-step Δt, data is calculated as mean values of 25 periods and divided by the length of the time-steps.

Controller	$W_{el}/\Delta t$	$W_{sys}/\Delta t$	$(\int \hat{Q}_a \dot{\theta})/\Delta t$	ω_q
Unit	Ws	Ws		Hz
$1M$-T	0.0020	0.0002	0.0002	3.0
$1M - E$	0.0020	0.0003	0.0003	2.9
$2M - V$	0.0080	0.0100	0.0080	4.7

pensated in one point is obviously identical for the same system $(u_{cmd} - u_{control})$, friction proportionally risis with velocity, which is why the $2M - V$ system shows higher physical friction work necessity μ_{obs}, due to higher velocities inbound. Here, it is important to take the calculation of μ_{obs} with a grain of salt, since the motor inertia influence is being neglected (Figure 4.4).

As already stated, the difference in frequency and speed of our pre-defined pick-and-place task can cause variations in results with respect to the length of the measured periods and their corresponding amount of time-steps Δt. To account for this time

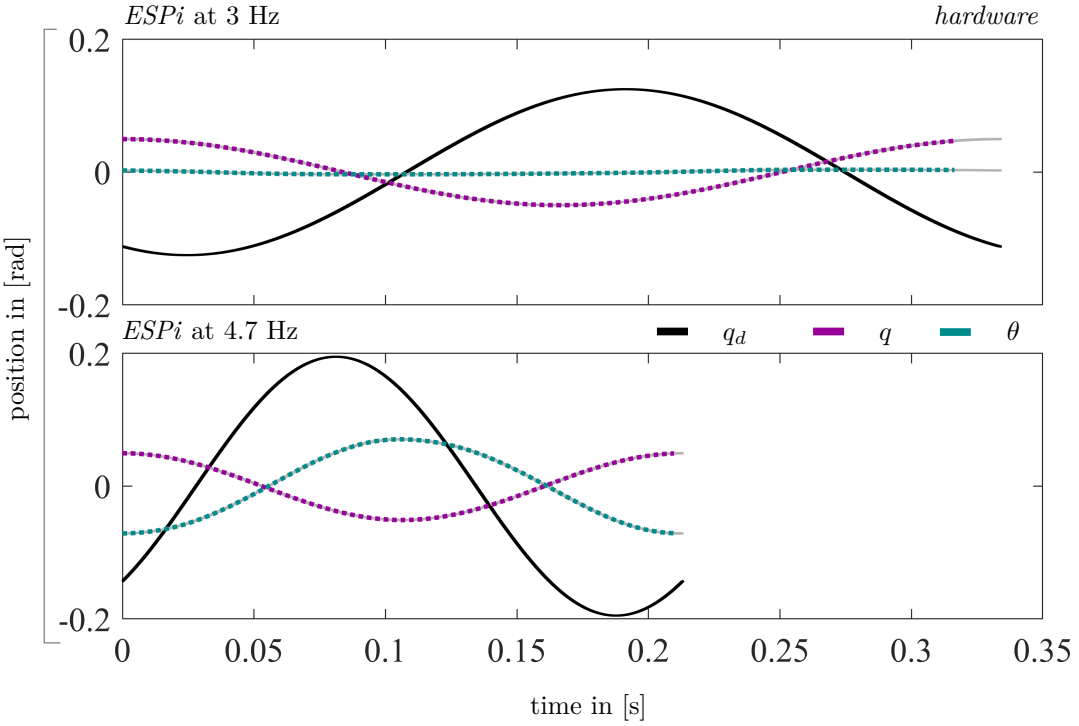

Figure 4.9: ESPi control for the two eigenfrequencies $\omega_{1D} = 3Hz$, $\omega_{2D} = 4.7Hz$, introducing q_d as the desired link position for tracking control, the $0.3Hz$ measurement is skipped for brevity ($\rightarrow$ *classical tracking*), further information can be drawn from here [12].

Table 4.7: Overall performance of the proposed ESPi experiments on hardware analyzed per period.

Controller	W_{el}/T	W_{sys}/T	$\hat{u}_{control}$	$\hat{u}_{cmd}$	μ_{obs}	$\varnothing\ i_{msr}$	ω_q
Unit	Ws	Ws	Nm	Nm	Ws	mA	Hz
ESPi	12.7	0.061	2.9	14.1	1.42	79.3	0.3
ESPi	2.0	0.163	20.8	37.6	0.21	121.8	3.0
ESPi	5.2	6.345	18.2	38.2	4.90	512.7	4.7

variation and compare the energy/ work that is added to the system in a fixed time, Table 4.6 shows relevant metrics normed per time-step of the respective period.

To compare the perfomance of the suggested control approaches with state-of-the-art controllers, the above presented values were calculated for the ESPi controlled motions. We start with the presentation of the ESPi measurements in Figure 4.9, where two of the mentioned frequency cases are presented. Table 4.7 gives an overview of the investigated perfomance metrics from before. The tracking mode of the ESPi with lowest frequencies shows high physical work consumption W_{el} per period, yet the observed precision of trajectory following is much higher ($\rightarrow$ *tracking control*). Also, with this approach little energy is added to the system boundary W_{sys} and yields only average performance concerning friction μ_{obs}. Nevertheless, this approach consumes by far less current than the other approaches. For the other two frequencies (3 Hz and 4.7 Hz), we see that the system is following the same behaviour.

5 Influence of Motor Inertia

This chapter seeks out to expand the presented control-ideas, regarding the influence of the motor mass in an single joint SEA system. Precisely, we want to investigate the $2M - V$ control approach in more detail, since here the mass of the motor is moving and bears the potential to shape the behavior of the controller. Therefore, we will alter the motor mass J_B through the principle of inertia shaping (Section 2.4) on hardware and simulation. To estimate how-far the inertia shaping reflects the behavior of a system with different parameters, we will change the physical mass properties in simulation.

5.1 Control Behavior with Inertia Shaping

Through implementation of the inertia shaping theory, we sweep the motor inertia from $J_{Bnew} = 0.25\ kg\,m^2$ to $J_{Bnew} = 2\ kg\,m^2$ with a fixed control of $E_{tot} \approx 1\ Ws$ (3.16) total energy. To maintain stability and facilitate analysis at the very low and high ends of the inertia shaping sweep, slight adjustments are made to the energy levels.

Figure 5.1 shows the investigated inertia shaping sweep. As apparent from the plots, the simulation and hardware results correspond well. Thus, in the following, we will only refer to the hardware results. As expected, for values close to the true value of the motor inertia $J_{Bnew} = 0.598\ kg\,m^2$, the motor behaves as seen in the previous controller coparison with the motor mass oscillating in anti-phase with the link mass. As the motor inertia is further increased, the deflection of the motor decreases, since the motor is more inert/ slow. Thus, the behavior becomes more similar to the behavior seen in the 1M-controllers, where the motor was set to remain in a fixed position. Table 5.1 shows the overall performance comparison of

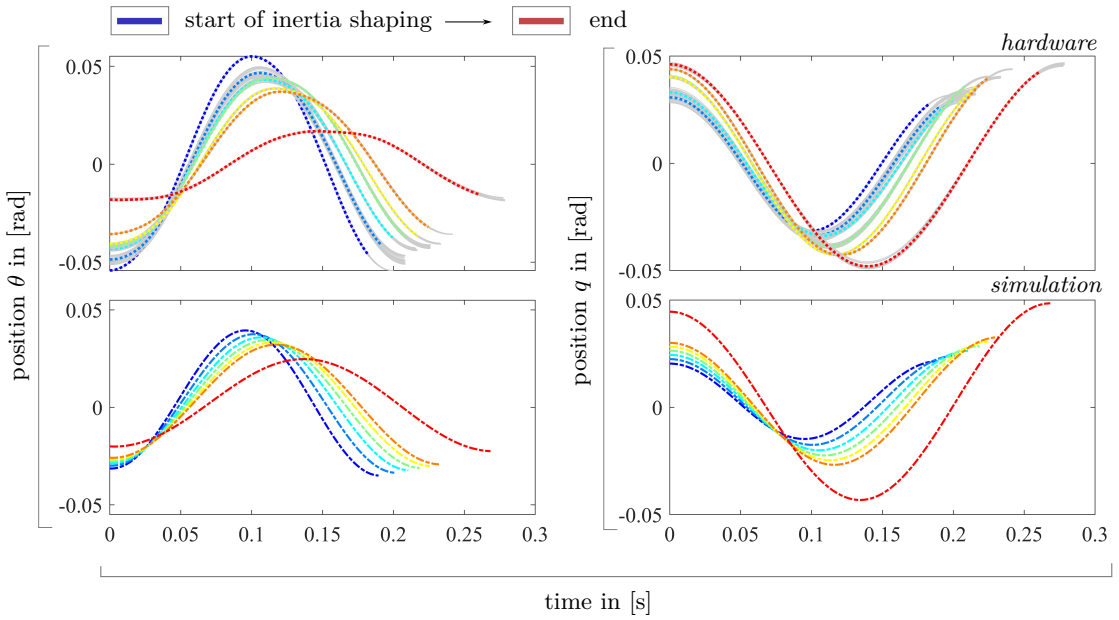

Figure 5.1: Inertia shaping sweep of J_B to J_{Bnew} on hardware with a fixed step of 0.1 $kg\,m^2$ from $J_{Bnew} = 0.5\ kg\,m^2$ (*blue*) to $J_{Bnew} = 1\ kg\,m^2$, plus $J_{Bnew} = 2\ kg\,m^2$ (*transistion to red*), mean values of 20 periods in *grey*.

the inertia sweep on the hardware. Since higher motor inertia is causing the motor to move less, the necessity for friction compensation is continously reduced, as well as the current consumption and the energy at system boundary. Moreover, we can see that the friction compensated torque amount (peak-to-peak) roughly stays the same. Also, note that the measurement plots are depicting anti-phasic ($\Delta\Phi_{ang} \approx \pi$) behaviour for all inertia shaped values. These observations point out the potential benefit of the 2M control approach to seemlessly shift between different control behaviors, which could be an advantage for some applications.

The highest inertia shaping value of $J_{Bnew} = 2\ kg\,m^2$ is purposely set to reach the 0.05 *rad* amplitude goal of the pick-and-place task, in order to enable comparison between the other 1M control approaches. Here, the link frequency ω_q is with 0.6 Hz slightly higher, yet the electric energy consumption per period is only 0.3 Ws higher and the system energy W_{sys} almost four times greater than compared to the $1M$-T and $1M - E$ approaches in Table 4.5. Clearly, the values in energy consumption do not differ much, yet enabling higher energies in the system.

Table 5.1: Inertia shaping sweep results on hardware for the $2M-V$ controller with E_{tot} as total energy of the system ($\rightarrow$ (3.16)), control goal: 1 Ws for J_{Bnew} from 0.6 $kg\,m^2$ until 1 $kg\,m^2$ and 0.05 rad amplitude for 2 $kg\,m^2$, see Section 4.1 and Section 4.2 for variable clarification.

J_{Bnew}	E_{tot}	ω_q	q	Δq	W_{el}/T	W_{sys}/T	$u_{control}$	u_{cmd}	μ_{obs}
$kg\,m^2$	Ws	Hz	rad	rad	Ws	Ws	Nm	Nm	
hardware									
0.25	1.4	5.0	0.032	-0.023	3.7	3.4	14.2	34.2	3.2
0.5	1.4	5.0	0.032	-0.023	3.7	3.5	14.0	34.0	3.2
0.6	1.1	4.8	0.034	-0.016	3.4	2.9	10.4	30.4	2.9
0.7	1.1	4.6	0.035	-0.010	3.2	2.5	8.2	28.2	2.6
0.8	1.1	4.4	0.040	-0.003	3.1	2.6	8.8	25.6	2.5
0.9	1.1	4.3	0.041	0.001	3.0	2.4	10.9	25.4	2.3
1.0	1.0	4.1	0.044	0.007	2.9	2.1	12.3	27.6	2.1
2.0	0.7	3.6	0.047	0.030	2.3	0.8	16.7	36.2	1.0

5.2 Control Behavior with Changed System Parameters

In order to investigate how well the inertia shaping alters the motor dynamics, in comparison to a system where the actual inertia differs, we seek out to get a glimpse of the $2M-V$ control approach regarding different testbed setups, where the motor inertia value J_B is changed through simulation. The following property sweep starts at very low inertia and ends up at 18 times the original inertia of 0.598 $kg\,m^2$.

To evaluate the performance of the motor inertia adjustment, we choose to set a fixed goal of 0.05 rad link-side amplitude, matching the original controller comparison experiment. The measurement results are depicted in Figure 5.2 and Table 5.2. As the mass is increased, the frequency, system-energy and commanded torque is decreased. Similar to the previous inertia shaping sweep, the motor position is

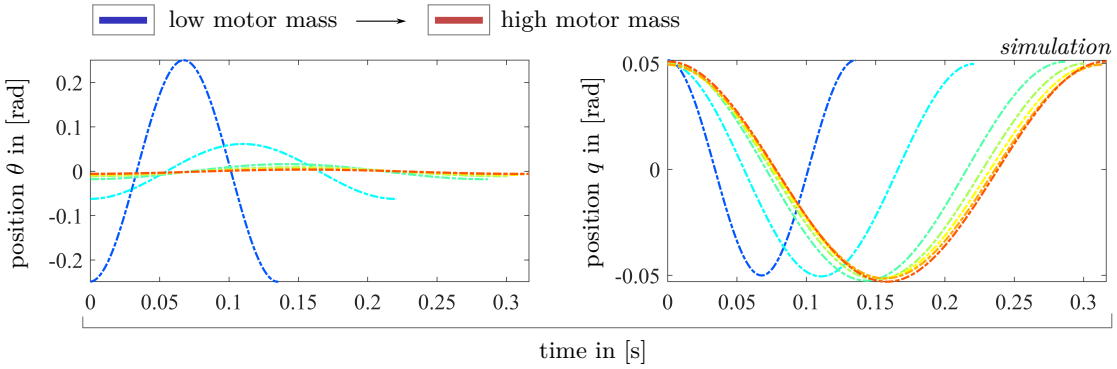

Figure 5.2: Modification of motor inertia properties in simulation of the SOFTY testbed, step size of sweep can be found in Table 5.2.

Table 5.2: Analysis of motor inertia property adjustment with a link-amplitude goal of $\hat{q} = 0.05\ rad$.

J_B	ω_q	$\hat{q}$	$\Delta\hat{q}$	W_{sys}/T	$\hat{u}_{control}$
$kg\,m^2$	Hz	rad	rad	Ws	Nm
0.2	7.4	0.051	-0.200	54.4	3.8
1.0	4.5	0.051	-0.012	5.0	0.9
3.0	3.5	0.050	0.035	0.9	0.8
5.0	3.3	0.050	0.041	0.5	1.0
7.0	3.2	0.049	0.043	0.3	1.1
9.0	3.2	0.049	0.045	0.2	1.4
11.0	3.2	0.050	0.047	0.2	1.6

reduced with higher motor inertia, causing the system to excite the link-side only and therefore reaching the characteristic 1D resonance frequency (ω_{1D}) of 3 Hz. In comparison to the altered motor mass through inertia shaping, quantitatively the same behavior can be observed. However, Table 5.2 reveals that changing the mass heavier than 3 $kg\,m^2$ does not lead to an increase in overall performance, since the motor inertia seems to saturate such that the behavior does not change further.

6 Discussion and Outlook

In the presented thesis we analyzed the behaviour of three different control approaches regarding two main concepts. The first concept was to excite a robotic system with one SEA-driven link in such a way that the motor is held stiff, whereas the link is excited to swing in its resonance frequency ($1M$-T and $1M-E$). The second concept was to not only excite the link-dynamics, but also exploit the inertia of the motor, in order to drive the SEA to swing in a combined frequency of both link- and motor-inertia ($2M-V$). To compare these controllers with different frequencies, a pick-and-place task was chosen with a fixed amplitude.

Consider Figure 6.1 for a final overview of the different controllers tested throughout this thesis. The initial case of 1D excitation approach ($1M$-T, $1M-E$, ESPi @$3Hz$) reveals to be more efficient for the considered pick-and-place task. Here, the spring is exploited via the link inertia solely and the link-side excitation is achieved through stiff motor-side actuation with normal mode movement of the link. Implementing 2D excitation on the robotic SOFTY testbed shows that for the given scenario a lot of friction arises $\int \hat{Q}_a \dot{\theta}$, which needs to be compensated adequately. Thus, for the given task and system the 1D-approach seems to be the better option, due to less friction, less current consumption W_{el} and effective energy exploitation with considerably fast link-side movement ω_q. This is due to the fact that friction rises proportionally to its velocity, hence the 1M-approaches causes less friction, since the motor is held almost static in this approach. As the necessity for friction compensation is reduced, the current consumption decreases respectively. Note that the $1M$-T and ESPi @$3Hz$ slightly outperform the $1M-E$ approach, due to a smoother signal regarding torque control and less stiff motor-side impedance. This particular observation can be traced back to the feedback term

of the virtual motor coordinate η of the $1M-E$, causing the system to behave in this manner. ESPi @$0.3Hz$, which applied a slow, yet almost ideal tracking of link- and motor position, produces slightly more friction than the 1D controlled systems, but nevertheless consumes less current than all the other controllers. Since the ESPi is applying tracking control, the motor is constantly moving to match the link position and hence producing more friction than when held stiff with the 1D approach. Nevertheless, the consumed current is lowest, since the motor is moving very slowly with little torque while the load with all other control approaches is much higher. Although the low current consumption of the ESPi @$0.3Hz$ could be initially seen as good performace, yet it needs to be considered that the system moves very slow and the elasticity of the system is not used at all. This also becomes apparent when regarding the performance metrics W_{el} and W_{sys}, which show little energy transfer to and in the system. Setting the ESPi frequency trajectory to the expected eigenfrequencies of the 1D and 2D system, i.e., 3 Hz and 4.7 Hz, the ESPi leads to similar control behavior, as seen for the investigated 1M- and 2M-controllers. Thus, it seems to be a valid approach to apply a control strategy that fits the intrinsic eigenfrequency of the system. However, it needs to be considered that, in more realistic scenarios with more complex systems the eigendynamics are most likely not known in advance.

The three controllers proposed in this thesis ($1M$-T, $1M-E$ & $2M-V$) automatically match the inherent dynamics and thus excite the system along its eigenfrequency without having to characterize the given system. Yet in order to apply the state-of-the-art ESPi, the eigenfrequency needs to be known in advance, to reach the identical beneficial control behaviors, which is unlikely for more complex systems. Thus, the proposed control approaches could, not only be used to drive the system, but also to characterize the system properties regarding the inherent dynamics.

It is important to note that for the 1M-controlled systems ($1M$-T, $1M-E$ and ESPi @$3Hz$), strong motor torques for fixing the motor position are neccessary, to counteract the forces of the fully swinging link. This implies, that the motor needs to be strong enough for the 1M-control approach to be applicable. Furthermore, the frequency of the task cannot be changed, as it solely depends on the link-side

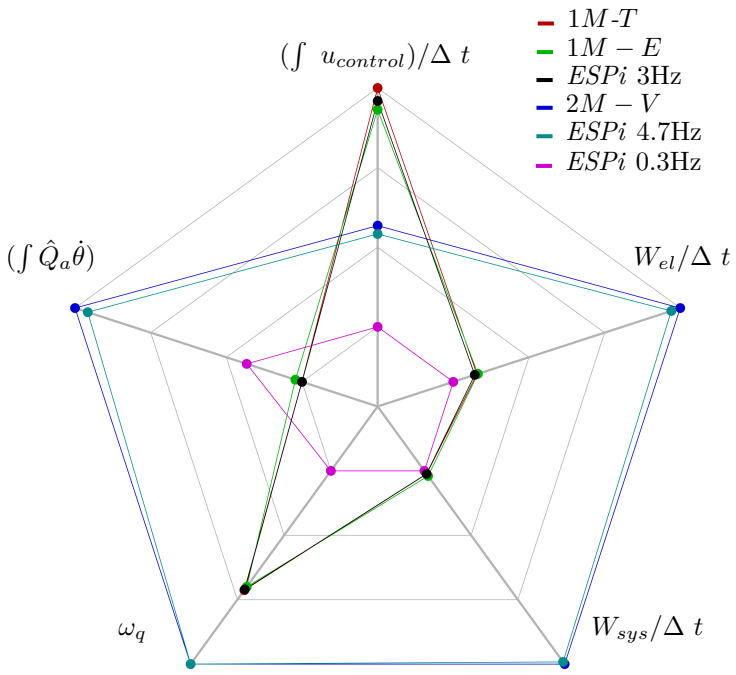

Figure 6.1: Spider plot for the key characteristics comparison of the proposed controllers: $\int \hat{Q}_a\dot{\theta} \rightarrow$ necessity for the level of friction compensation (high values indicating low friction performance), $\int u_{control} \rightarrow$ produced torque of the controllers without friction compensation, $W_{el} \rightarrow$ physical work of electric consumption, $W_{sys} \rightarrow$ system energy between spring and motor, $\omega_q \rightarrow$ link frequency of oscillation, all energy measurements are analyzed per timestep Δt of one mean period T.

dynamics, but can suit various other taks, e.g. assembly lines, where everything is synced and should not change in its pattern.

The $2M-V$ approach seems to be able to add much more energy to the system than the 1M-controllers. This appears disadvantageous for the chosen task of reaching a fixed amplitude in a pick-and-place scenario, as much of the energy is not put to use and unnecessarily added. Nevertheless, the ability to add more energy in a system, by additionally deflecting the motor, could be beneficial for other applications, e.g. mobile robots with high explosive movement. As the second experiment indicated (Chapter 5), inertia shaping can be used to change the behavior of the controller and add flexibility to the control strategy. The 2D-behaviour can

be shifted towards 1D, when the virtual motor inertia is increased, showing similar characteristics and results as the 1M-approaches. The frequency and amplitude can be adjusted to suit a task-specific purpose. This could be useful in work stations of small- and medium-sized enterprises, where one assembly setup might be used for different tasks, such that a more adaptable and flexible controller might be beneficial to avoid hardware adjustments.

Additionally, the limitations of the carried out study need to be acknowledged. Only one specific system, i.e. a single one-link SEA testbed driven through an actuator with a harmonic drive, was investigated. Note that only steady-state behavior was analyzed and the rise time was not considered, although it could be important depending on the desired task. Also, no forces have been exerted on the link with no object transport per se. This should be additionally investigated when regarding the herein presented results. In future studies and research the controllers could be applied to a variety of actuator concepts with different motors and gears, in order to gain an insight on more generic system behavior and application. Also, planetary gears with potential recuperation represent a valid investigation, since the reversible energy of the motor swing could be exploited in beneficial ways. Furthermore, there are various tasks and scenarios that could be investigated, e.g. different trajectories with multiple forces acting on the system (coriolis-, gravity-forces, etc.). As the main three controllers from this thesis follow eigendynamics excitation, extending the controllers to a multi-joint system is another big challenge that needs to be addressed in future research. More realistic, less perfect non-lab scenarios should be investigated, to unveil the true potential of the tested control approaches.

Although this thesis only was a first step to investigate control strategies that exploit the intrinsic dynamics of a system, by additionally taking into account the motor dynamics, the results reveal potential for further and more extensive investigations. It is imaginable that a combination of the investigated control strategies shifting between the utilization of complete system dynamics, compared to link-side dynamics solely, could extend capabilities in control of various system applications. It could be advantageous to combine different approaches for robotic locomotion [45] [46]. Notably, the 2D approach can be uniquely beneficial, as it seems capable to inject a lot of energy, which could be channeled into explosive

movements in SEAs and VSAs. Paired with artificial intelligence and reinforcement learning techniques the investigated control ideas could improve locomotion or system identification, specifically when coupled with harmonic oscillatory excitation are required for a task. This way, control of different inertia shaped properties for the 2D-approach could be further optimized with direct task dependency, optimally exploiting the eigendynamics of a system and automatically choosing the best suited control during motion.

7 Conclusion

The presented research study investigated the potential of eigendynamics exploitation in SEA driven robots with one link, introducing the novelty of including the motor-inertia as part of the control concept to excite an oscillation for a pick-and-place-task. It was found that although the inclusion of the motor inertia bears the potential to add more energy to the system, the increased velocity of the motor also leads to a proportional increase in friction that needs to be compensated. Additionally applying inertia shaping, showed that the behavior of the 2M-controller could be easily adapted. In this way, the system could be shaped such that the motor either behaved more statically, i.e., causing less friction and efficiently using the spring, or more dynamically, where more energy could be added to the system. These findings form first important insights to the potential of exploiting motor inertia in control strategies. This could eventually aid to develop a flexible control approach for compliant robots that can be energy-efficient while at the same time being able to carry out explosive movements when needed.

References

[1] Rainer Bischoff, Johannes Kurth, Guenter Schreiber, Ralf Koeppe, Alin Albu-Schaeffer, Alexander Beyer, Oliver Eiberger, Sami Haddadin, Andreas Stemmer, Gerhard Grunwald, and Gerhard Hirzinger. The kuka-dlr lightweight robot arm - a new reference platform for robotics research and manufacturing. In *ISR 2010 (41st International Symposium on Robotics) and ROBOTIK 2010 (6th German Conference on Robotics)*, pages 1–8, 2010.

[2] Alaa Saadah, Maria Al Kadi, and Husi Géza. Kuka arc kr5 industrial manipulator's trajectory planning modelling using matlab based on kinematics study. In *2023 Advances in Science and Engineering Technology International Conferences (ASET)*, pages 01–06, 2023. doi: 10.1109/ASET56582.2023.10180693.

[3] Jessica Burgner-Kahrs, D. Caleb Rucker, and Howie Choset. Continuum robots for medical applications: A survey. *IEEE Transactions on Robotics*, 31 (6):1261–1280, 2015. doi: 10.1109/TRO.2015.2489500.

[4] Nicola Vitiello, Tommaso Lenzi, Stefano Roccella, Stefano Marco Maria De Rossi, Emanuele Cattin, Francesco Giovacchini, Fabrizio Vecchi, and Maria Chiara Carrozza. Neuroexos: A powered elbow exoskeleton for physical rehabilitation. *IEEE Transactions on Robotics*, 29(1):220–235, 2013. doi: 10.1109/TRO.2012.2211492.

[5] Sai K. Banala, Seok Hun Kim, Sunil K. Agrawal, and John P. Scholz. Robot assisted gait training with active leg exoskeleton (alex). In *2008 2nd IEEE RAS & EMBS International Conference on Biomedical Robotics and Biomechatronics*, pages 653–658, 2008. doi: 10.1109/BIOROB.2008.4762885.

[6] Libo Meng, Zhangguo Yu, Xuechao Chen, Weimin Zhang, Marco Ceccarelli,

Kenji Hashimoto, Atsuo Takanishi, Qiang Huang, Wenjuan Guo, Lin Xie, and Huaxin Liu. A falling motion control of humanoid robots based on biomechanical evaluation of falling down of humans. In *2015 IEEE-RAS 15th International Conference on Humanoid Robots (Humanoids)*, pages 441–446, 2015. doi: 10.1109/HUMANOIDS.2015.7363571.

[7] Georg Wiedebach, Sylvain Bertrand, Tingfan Wu, Luca Fiorio, Stephen McCrory, Robert Griffin, Francesco Nori, and Jerry Pratt. Walking on partial footholds including line contacts with the humanoid robot atlas. In *2016 IEEE-RAS 16th International Conference on Humanoid Robots (Humanoids)*, pages 1312–1319, 2016. doi: 10.1109/HUMANOIDS.2016.7803439.

[8] David Wooden, Matthew Malchano, Kevin Blankespoor, Andrew Howardy, Alfred A. Rizzi, and Marc Raibert. Autonomous navigation for bigdog. In *2010 IEEE International Conference on Robotics and Automation*, pages 4736–4741, 2010. doi: 10.1109/ROBOT.2010.5509226.

[9] Amanda Bouman, Muhammad Fadhil Ginting, Nikhilesh Alatur, Matteo Palieri, David D. Fan, Thomas Touma, Torkom Pailevanian, Sung-Kyun Kim, Kyohei Otsu, Joel Burdick, and Ali-akbar Agha-Mohammadi. Autonomous spot: Long-range autonomous exploration of extreme environments with legged locomotion. In *2020 IEEE/RSJ International Conference on Intelligent Robots and Systems (IROS)*, pages 2518–2525, 2020. doi: 10.1109/IROS45743.2020.9341361.

[10] Sangok Seok, Albert Wang, Meng Yee Chuah, David Otten, Jeffrey Lang, and Sangbae Kim. Design principles for highly efficient quadrupeds and implementation on the mit cheetah robot. In *2013 IEEE International Conference on Robotics and Automation*, pages 3307–3312, 2013. doi: 10.1109/ICRA.2013.6631038.

[11] Jared Di Carlo, Patrick M. Wensing, Benjamin Katz, Gerardo Bledt, and Sangbae Kim. Dynamic locomotion in the mit cheetah 3 through convex model-predictive control. In *2018 IEEE/RSJ International Conference on Intelligent Robots and Systems (IROS)*, pages 1–9, 2018. doi: 10.1109/IROS.2018.8594448.

[12] Manuel Keppler, Dominic Lakatos, Christian Ott, and Alin Albu-Schaffer. Elastic structure preserving impedance (ESπ) control for compliantly actuated robots. In *2018 IEEE/RSJ International Conference on Intelligent Robots and Systems (IROS)*, pages 5861–5868, 2018. doi: 10.1109/IROS.2018.8593415.

[13] Filip Bjelonic, Arne Sachtler, Alin Albu-Schäffer, and Cosimo Della Santina. Experimental closed-loop excitation of nonlinear normal modes on an elastic industrial robot. *IEEE Robotics and Automation Letters*, 7(2):1689–1696, 2022. doi: 10.1109/LRA.2022.3141156.

[14] Davide Calzolari, Cosimo Della Santina, Alessandro M. Giordano, and Alin Albu-Schäffer. Single-leg forward hopping via nonlinear modes. In *2022 American Control Conference (ACC)*, pages 506–513, 2022. doi: 10.23919/ACC53348.2022.9867538.

[15] Dominic Lakatos, Kai Ploeger, Florian Loeffl, Daniel Seidel, Florian Schmidt, Thomas Gumpert, Freia John, Torsten Bertram, and Alin Albu-Schäffer. Dynamic locomotion gaits of a compliantly actuated quadruped with slip-like articulated legs embodied in the mechanical design. *IEEE Robotics and Automation Letters*, 3(4):3908–3915, 2018. doi: 10.1109/LRA.2018.2857511.

[16] Ojiro Matsumoto, Shunsuke Shigaki, Shuhei Ikemoto, Tsung-Yuan Chen, Masahiro Shimizu, and Koh Hosoda. 2dof link mechanism mimicking cheetah's spine and leg movement. In *2019 IEEE International Conference on Robotics and Biomimetics (ROBIO)*, pages 120–125, 2019. doi: 10.1109/ROBIO49542.2019.8961719.

[17] Boston dynamics cheetah robot now faster than fastest human. https://spectrum.ieee.org/boston-dynamics-cheetah-robot-now-faster-than-fastest-human, 2012. Accessed: 2023-09-01.

[18] Mathew Jose Pollayil, Cosimo Della Santina, George Mesesan, Johannes Englsberger, Daniel Seidel, Manolo Garabini, Christian Ott, Antonio Bicchi, and Alin Albu-Schaffer. Planning natural locomotion for articulated soft quadrupeds. In *2022 International Conference on Robotics and Automation (ICRA)*, pages 6593–6599, 2022. doi: 10.1109/ICRA46639.2022.9812416.

[19] Hansol Song, Yun-Soo Kim, Junsuk Yoon, Seong-Ho Yun, Jiwon Seo, and Yong-Jae Kim. Development of low-inertia high-stiffness manipulator lims2 for high-speed manipulation of foldable objects. In *2018 IEEE/RSJ International Conference on Intelligent Robots and Systems (IROS)*, pages 4145–4151, 2018. doi: 10.1109/IROS.2018.8594005.

[20] Patrick M. Wensing, Albert Wang, Sangok Seok, David Otten, Jeffrey Lang, and Sangbae Kim. Proprioceptive actuator design in the mit cheetah: Impact mitigation and high-bandwidth physical interaction for dynamic legged robots. *IEEE Transactions on Robotics*, 33(3):509–522, 2017. doi: 10.1109/TRO.2016.2640183.

[21] Gerardo Bledt, Matthew J. Powell, Benjamin Katz, Jared Di Carlo, Patrick M. Wensing, and Sangbae Kim. Mit cheetah 3: Design and control of a robust, dynamic quadruped robot. In *2018 IEEE/RSJ International Conference on Intelligent Robots and Systems (IROS)*, pages 2245–2252, 2018. doi: 10.1109/IROS.2018.8593885.

[22] Quan Nguyen, Matthew J. Powell, Benjamin Katz, Jared Di Carlo, and Sangbae Kim. Optimized jumping on the mit cheetah 3 robot. In *2019 International Conference on Robotics and Automation (ICRA)*, pages 7448–7454, 2019. doi: 10.1109/ICRA.2019.8794449.

[23] Maged Iskandar, Christiaan van Ommeren, Xuwei Wu, Alin Albu-Schäffer, and Alexander Dietrich. Model predictive control applied to different time-scale dynamics of flexible joint robots. *IEEE Robotics and Automation Letters*, 8(2):672–679, 2023. doi: 10.1109/LRA.2022.3229226.

[24] Daniel Seidel, Milan Hermann, Thomas Gumpert, Florian Christoph Loeffl, and Alin Albu-Schäffer. Using elastically actuated legged robots in rough terrain: Experiments with dlr quadruped bert. In *2020 IEEE Aerospace Conference, AERO 2020*, pages 1–8. IEEE, März 2020. URL https://elib.dlr.de/139409/.

[25] Markus Grebenstein, Alin Albu-Schäffer, Thomas Bahls, Maxime Chalon, Oliver Eiberger, Werner Friedl, Robin Gruber, Sami Haddadin, Ulrich Hagn, Robert Haslinger, Hannes Höppner, Stefan Jörg, Mathias Nickl, Alexander Nothhelfer, Florian Petit, Josef Reill, Nikolaus Seitz, Thomas Wimböck,

Sebastian Wolf, Tilo Wüsthoff, and Gerd Hirzinger. The dlr hand arm system. In *2011 IEEE International Conference on Robotics and Automation*, pages 3175–3182, 2011. doi: 10.1109/ICRA.2011.5980371.

[26] David Braun, Matthew Howard, and Sethu Vijayakumar. Exploiting variable stiffness in explosive movement tasks. In *Robotics: Science and Systems*, page 9, 06 2011. doi: 10.15607/RSS.2011.VII.004.

[27] Christian Ott. *Cartesian Impedance Control of Redundant and Flexible-Joint Robots*. Springer Publishing Company, Incorporated, 1 edition, 2008. ISBN 3540692533.

[28] M. W. Spong. Modeling and control of elastic joint robots. *Journal of Dynamic Systems, Measurement, and Control*, 109(4):310–318, 1987. ISSN 0022-0434. doi: 10.1115/1.3143860.

[29] C. Ott, A. Albu-Schaffer, A. Kugi, S. Stamigioli, and G. Hirzinger. A passivity based cartesian impedance controller for flexible joint robots - part i: torque feedback and gravity compensation. In *IEEE International Conference on Robotics and Automation, 2004. Proceedings. ICRA '04. 2004*, volume 3, pages 2659–2665 Vol.3, 2004. doi: 10.1109/ROBOT.2004.1307462.

[30] Manuel Keppler, Dominic Lakatos, Christian Ott, and Alin Albu-Schäffer. A passivity-based controller for motion tracking and damping assignment for compliantly actuated robots. In *IEEE Conference on Decision and Control*, pages 1521–1528, Dezember 2016. URL https://elib.dlr.de/110670/.

[31] George Jose Pollayil, Xuming Meng, Manuel Keppler, Martin Pfanne, Antonio Bicchi, and Christian Ott. Elastic structure preserving impedance control for nonlinearly coupled tendon-driven systems. *IEEE Control Systems Letters*, 6: 1982–1987, 2022. doi: 10.1109/LCSYS.2021.3136749.

[32] Manuel Keppler, Florian Loeffl, David Wandinger, Clara Raschel, and Christian Ott. Analyzing the performance limits of articulated soft robots based on the espi framework: Applications to damping and impedance control. *IEEE Robotics and Automation Letters*, 6(4):7121–7128, 2021. doi: 10.1109/LRA.2021.3097079.

[33] Xuming Meng, Manuel Keppler, and Christian Ott. Elastic structure preserving impedance control of bidirectional antagonistic variable stiffness actuation. In *2021 European Control Conference (ECC)*, pages 263–269, 2021. doi: 10.23919/ECC54610.2021.9655122.

[34] Dominic Lakatos, Florian Petit, and Alin Albu-Schäffer. Nonlinear oscillations for cyclic movements in human and robotic arms. *IEEE Transactions on Robotics*, 30(4):865–879, August 2014. URL https://elib.dlr.de/89442/.

[35] Annika Schmidt, Benedikt Feldotto, Thomas Gumpert, Daniel Seidel, Alin Albu-Schäffer, and Philipp Stratmann. Adapting highly-dynamic compliant movements to changing environments: A benchmark comparison of reflex- vs. cpg-based control strategies. *Frontiers in Neurorobotics*, 15, 2021. ISSN 1662-5218. doi: 10.3389/fnbot.2021.762431. URL https://www.frontiersin.org/articles/10.3389/fnbot.2021.762431.

[36] Dominic Lakatos, Daniel Seidel, Werner Friedl, and Alin Albu-Schäffer. Targeted jumping of compliantly actuated hoppers based on discrete planning and switching control. In *2015 IEEE/RSJ International Conference on Intelligent Robots and Systems (IROS)*, pages 5802–5808, 2015. doi: 10.1109/IROS.2015.7354201.

[37] J.V. José and E.J. Saletan. *Classical Dynamics: A Contemporary Approach*. Cambridge University Press, 1998. ISBN 9780521636360. URL https://books.google.de/books?id=Eql9dRQDgvQC.

[38] D. Morin. *Introduction to Classical Mechanics: With Problems and Solutions*. Cambridge University Press, 2008. ISBN 9780521876223. URL https://books.google.de/books?id=uRmBngEACAAJ.

[39] Alin Albu-Schäffer and Cosimo Della Santina. A review on nonlinear modes in conservative mechanical systems. *Annual Reviews in Control*, 50:49–71, 2020. ISSN 1367-5788. doi: https://doi.org/10.1016/j.arcontrol.2020.10.002. URL https://www.sciencedirect.com/science/article/pii/S1367578820300687.

[40] Christian Ott, Alin Albu-Schaffer, Andreas Kugi, and Gerd Hirzinger. On the passivity-based impedance control of flexible joint robots. *IEEE Transactions on Robotics*, 24(2):416–429, 2008. doi: 10.1109/TRO.2008.915438.

[41] Alexander Dietrich, Xuwei Wu, Kristin Bussmann, Marie Harder, Maged Iskandar, Johannes Englsberger, Christian Ott, and Alin Albu-Schäffer. Practical consequences of inertia shaping for interaction and tracking in robot control. *Control Engineering Practice*, 114:104875, 2021. ISSN 0967-0661. doi: https://doi.org/10.1016/j.conengprac.2021.104875. URL https://www.sciencedirect.com/science/article/pii/S0967066121001520.

[42] Manuel Keppler and Alessandro Luca. On time-optimal control of elastic joints under input constraints. In *2020 59th IEEE Conference on Decision and Control (CDC)*, pages 4149–4156, 12 2020. doi: 10.1109/CDC42340.2020.9304224.

[43] David Wandinger. Enhancing classical impedance control concepts while ensuring transferability to flexible joint robots. Technical report, Hochschule München, September 2020. URL https://elib.dlr.de/139129/.

[44] Luc Le Tien, Alin Albu-Schaffer, Alessandro De Luca, and Gerd Hirzinger. Friction observer and compensation for control of robots with joint torque measurement. In *2008 IEEE/RSJ International Conference on Intelligent Robots and Systems*, pages 3789–3795, 2008. doi: 10.1109/IROS.2008.4651049.

[45] Donald Hoyt and C. Taylor. Gait and the energetic of locomotion in horses. *Nature*, 292:239–240, 07 1981. doi: 10.1038/292239a0.

[46] Vance A. Tucker. The energetic cost of moving about. *American scientist*, 63 4:413–9, 1975. URL https://api.semanticscholar.org/CorpusID:37169992.

ERKLÄRUNG

gemäß §15 Abs. 5 APO in Zusammenhang mit §35 Abs. 7 Rapo

Name	Filip Pasic
Geburtsdatum	09.04.1997
Studiengang	M.Sc. Elektrotechnik
Matrikel-Nr.	19193516
Zeitraum	15.03.2023 - 15.09.2023
Betreuer @ HM	Prof. Dr. Christoph M. Hackl
Betreuer @ DLR	M.Sc.-Ing. Annika Schmidt
	Prof. Dr. Alin Albu-Schäffer

Hiermit erkläre ich, das ich die Masterarbeit selbständig verfasst, noch nicht anderweitig für Prüfungszwecke vorgelegt, keine anderen als die angegeben Quellen oder Hilfsmittel benutzt, sowie wörtliche und sinngemäße Zitate als solche gekennzeichnet habe.

München, 03.09.2023

Ort, Datum

Unterschrift